Near-fault Strong-motion of the 2023 Mw7.8 Kahramanmaraş Earthquake: Insights into High-frequency Radiation Mechanisms

Baoning Wu[1,2], Bo Li[3], Hao Zhang[2], Shuye Huang[2], Guoliang Li[2,4], and Alice-Agnes Gabriel[1,5]

[1]Scripps Institution of Oceanography, University of California, San Diego, USA
[2]Department of Earth Sciences, University of Southern California, USA
[3]Physical Science and Engineering Division, King Abdullah University of Science and Technology, Saudi Arabia
[4]School of Geosciences and Info-Physics, Central South University, China
[5]Department of Earth and Environmental Sciences, Ludwig Maximilian University of Munich, Germany

Key Points:

- We observe a loss of polarity and reduced coherence above ~ 0.4 Hz in near-fault records of 2023 Mw 7.8 Kahramanmaraş earthquake.
- The ~ 0.4 Hz transition frequency is lower than the commonly accepted rule-of-thumb value of 1 Hz.
- Our results highlight the need for improved earthquake source parameterization to assess high-frequency ground motion hazards.

Corresponding author: Baoning Wu, `baw011@ucsd.edu`

Abstract

While classic double-couple earthquake models explain seismic wavefields accurately at low frequencies, at higher frequencies, seismic radiation exhibits significantly more complex and stochastic characteristics. Various on-fault and off-fault mechanisms have been proposed to explain high-frequency radiation, yet their relative contributions and trade-offs remain debated. In this study, we analyze near-fault high-frequency characteristics of the 2023 Mw 7.8 Kahramanmaraş earthquake with 19 strong-motion stations within 10 km of its southern rupture. Above ~ 0.4 Hz, we observe a loss of horizontal polarity and reduced coherence between the two horizontal components, which cannot be explained by heterogeneous rupture on a planar fault. Additionally, the $\sim$ 0.4 Hz transition frequency is lower than the commonly accepted rule-of-thumb value of 1 Hz. The near-fault high-frequency energy arrives concurrently with low-frequency signals, suggesting that high-frequency radiation originates near the fault rather than from medium scattering. Comparison with regional stations and back-projection analysis suggests that high-frequency signatures from the source persist even at greater distances. These findings indicate that the small-scale radiation processes near the rupture front are more complex than those described in conventional earthquake source representations. Our results highlight the need for improved earthquake source parameterization to assess high-frequency ground motion hazards and may provide valuable constraints for theoretical studies on high-frequency radiation mechanisms.

Plain Language Summary

Classic earthquake models can accurately explain the seismic wavefield below an earthquake's corner frequency. However, at higher frequencies, seismic radiation exhibits significantly more complex and stochastic characteristics. While various types of on-fault and off-fault complexity have been proposed to generate high-frequency radiation, their respective contributions and trade-offs remain the subject of ongoing debate. The 2023 magnitude 7.8 Kahramanmaraş earthquake was well recorded by the regional strong-motion network operated by the Turkey Disaster and Emergency Management Authority (AFAD). About 20 three-component accelerometers are located within 10 km of the EAF surface rupture south of the Narlı-EAF junction. These stations span rather evenly along the fault strike, recording seismic radiation from the rupture front as it propagated southward. This dataset provides an excellent opportunity to investigate how high-frequency radiation is generated at earthquake sources. We observe a loss of horizontal polarity and reduced coherence above approximately 0.4 Hz in these records, which we argue cannot be fully explained by traditional models of heterogeneous rupture parameters on a planar fault. Our findings demonstrate the need for improved earthquake source parameterization to assess high-frequency ground motion hazards and may provide valuable insights for theoretical studies on high-frequency radiation mechanisms.

1 Introduction

Understanding earthquake high-frequency radiation is crucial for characterizing its earthquake processes and its hazards (Aki, 2003). Classic earthquake models with simplified rupture processes can adequately explain the seismic wavefield below the earthquake corner frequency (e.g., Haskell, 1964; Aki, 1967; Brune, 1970; Madariaga, 1976). However, at higher frequencies, seismic radiation becomes markedly more complex and stochastic (e.g., Housner, 1947; Hanks & McGuire, 1981). While classical models may predict the amplitude of high-frequency spectra, they often fail to account for other features, such as waveform coherence (e.g., Hanks, 1979; Hanks & McGuire, 1981; Boore, 1983) and ground motion polarity (e.g., Somerville et al., 1997; Graves & Pitarka, 2016; Ben-Zion et al., 2024). Accurately modeling these high-frequency radiation features is desirable, as they could be crucial for specific structural designs aimed at mitigating earthquake ground motion hazards.

It is generally agreed that high-frequency radiation reflects spatial complexities in the source or path that are smaller than the source dimension (e.g., Lay et al., 2012). However, many types of complexity could contribute to high-frequency radiation, including heterogeneous rupture on a planar fault (e.g., Madariaga, 1977; Spudich & Frazer, 1984; Zeng et al., 1994), complex fault geometry (e.g., Adda-Bedia & Madariaga, 2008; Shi & Day, 2013), small off-fault structures or damage (e.g., Ben-Zion & Ampuero, 2009), low velocity fault damage zone (e.g., Graves & Pitarka, 2016), scattering bodies around fault (e.g., Imperatori & Mai, 2012), and complex fault gouge structures (e.g., Tsai & Hirth, 2020). Their actual contributions remain poorly understood due to limited observational constraints near the fault.

The 2023 Mw 7.8 Kahramanmaraş earthquake caused tens of thousands of casualties and widespread devastation (e.g., Erdik et al., 2023). It also provides a unique opportunity to study high-frequency radiation mechanisms. It was the first event of a doublet that ruptured the East Anatolian Fault (EAF) system on February 6, 2023 (UTC). Thanks to the high-quality data from near-fault, regional, and global observatories, the Mw 7.8 earthquake has been extensively characterized in numerous studies (e.g., Barbot et al., 2023; Melgar et al., 2023; Reitman, Briggs, Barnhart, Hatem, et al., 2023; Y. Zhang et al., 2023; Mai et al., 2023; Jia et al., 2023; Güvercin, 2024; Akinci et al., 2025). In particular, around 20 three-component strong motion accelerometers were located within 10 km of the approximately 100 km-long southern EAF rupture (e.g., Palo & Zollo, 2024; Ren et al., 2024; S. Yao & Yang, 2025). Due to the proximity of these stations, the recorded seismic radiation is minimally influenced by crustal scattering, making it an ideal dataset to study high-frequency radiation mechanisms at the source.

In this study, we address high-frequency radiation mechanisms with these near-fault acceleration records. We first examined how the ratio of fault-normal (FN) to fault-parallel (FP) components changes with frequency. Most FN/FP ratios are greater than unity below $\sim$ 0.4 Hz, consistent with the expected behavior for an overall sub-shear rupture (e.g., Dunham & Archuleta, 2005; Mello et al., 2016; Abdelmeguid et al., 2023). However, FN/FP ratios approach unity above $\sim$ 0.4 Hz, suggesting a loss of horizontal polarity. We also analyzed how signal coherence changes with frequency. We observed that the correlation coefficient between two horizontal components decreases from near unity to zero as frequency increases, also at a transition frequency of $\sim$ 0.4 Hz.

Spectrograms of these records indicate that most high-frequency energy coincides with the arrival of low-frequency signals, suggesting that near-fault complexities are the primary source of high-frequency radiation, rather than medium scattering away from the fault. Our result, showing a $\sim$ 0.4 Hz transition frequency, suggests that source complexities may persist in wavelengths up to a few kilometers. We discuss the possible mechanisms underlying the high-frequency radiation observations. We suggest that these source complexities are likely related to the heterogeneous 3D structure near the fault, and that the observed high-frequency radiation cannot be fully modeled by simply parameterizing inhomogeneous friction or stress on a planar fault.

2 Simultaneous Arrivals of High- and Low-Frequency Radiation

The rupture process of the Mw 7.8 earthquake has been well characterized by multiple datasets (e.g., Melgar et al., 2023; Mai et al., 2023; Reitman, Briggs, Barnhart, Hatem, et al., 2023; Jia et al., 2023; Y. Zhang et al., 2023; C. Liu et al., 2023; Ren et al., 2024). The rupture initiated on the Narlı fault, a secondary strand of the EAF system, and reached the Narlı-EAF junction in about 10 seconds (Figure 1a). The rupture then continued propagating bilaterally from the junction. The south-propagating rupture beyond the

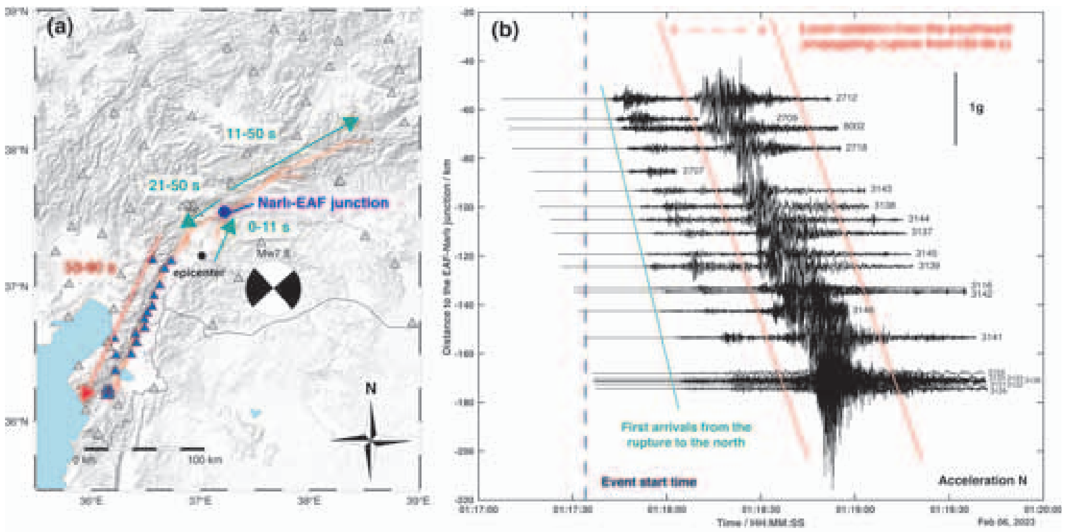

Figure 1. **(a)** Map showing regional strong-motion stations close to the Mw 7.8 earthquake surface ruptures (red lines). The surface rupture data were obtained from the `simple_fault` files within the fault rupture mapping dataset provided by Reitman, Briggs, Barnhart, Thompson Jobe, et al. (2023). Blue triangles represent the 22 stations within 10 km of the southern surface rupture. Grey triangles represent other regional strong-motion stations. Arrows show the coseismic rupture process inferred by Jia et al. (2023), with corresponding rupture times labeled. The red arrow denotes the south-propagating rupture that this study focuses on. **(b)** North-south component unfiltered accelerograms of the 22 strong-motion stations (blue triangles in (a)) within 10 km of the southern surface rupture ordered by the distance from the station to the Narlı-EAF junction, taking north as the positive direction.

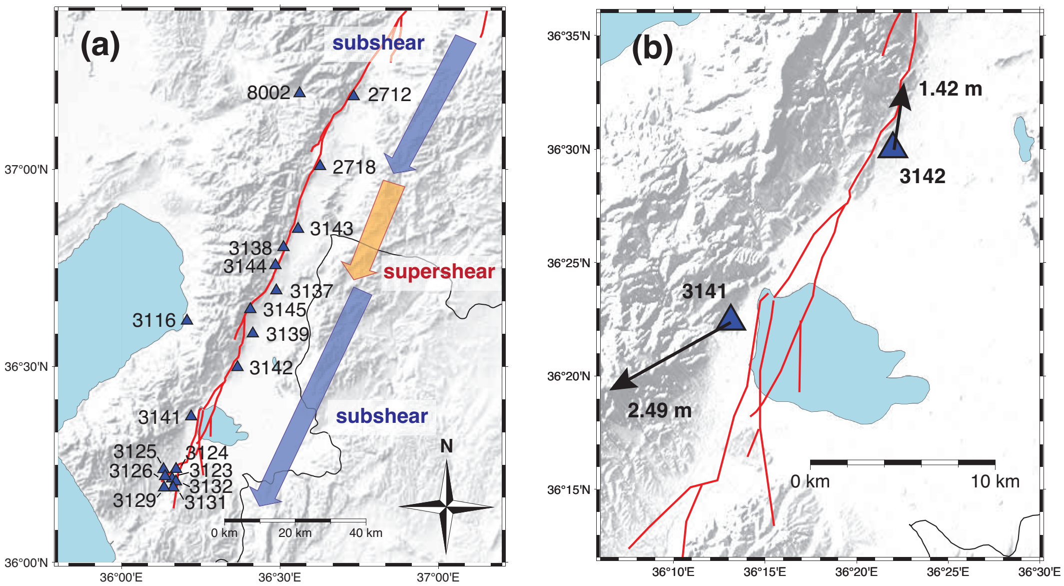

Figure 2. **(a)** Map showing the 19 regional strong-motion stations (blue triangles) near the Mw 7.8 earthquake surface ruptures (red lines), which recorded the complete rupture front radiation as it propagated southward. Arrows highlight the approximate portions of subshear (blue) and supershear (yellow) rupture, as reported by S. Yao and Yang (2025). **(b)** Map showing the locations of Stations 3141 and 3142 (blue triangles) relative to the surface rupture (red lines). Black arrows and corresponding labels indicate the final horizontal displacements, obtained by double-integrating the acceleration records. The surface rupture data were obtained from the `simple_fault` files within the fault rupture mapping dataset provided by Reitman, Briggs, Barnhart, Thompson Jobe, et al. (2023).

fault bend was delayed and reactivated around 50 seconds after the initial rupture. The rupture delay is probably due to this earthquake's specific fault geometry and pre-stress level (Gabriel et al., 2023; Ding et al., 2023).

The Mw 7.8 earthquake was well recorded by the regional three-component strong-motion stations, with 22 stations within 10 km of the southern rupture (Figure 1a). These stations are relatively evenly spaced along the fault trace. Figure 1b shows the north-south component acceleration recorded by these 22 stations.

The first arrival in these records is radiation from the initial rupture to the north. In general, the amplitude of these waves decreases with the distance to the Narlı-EAF junction. Following the initial motion is a stronger pulse with a duration of about 30 seconds, which is radiation from the marching rupture front (e.g., Čejka et al., 2023; Nagasaka & Nozu, 2024; Ren et al., 2024; Palo & Zollo, 2024; S. Yao & Yang, 2025; Yen et al., 2025), and the pulse amplitude does not decrease with the distance to the Narlı-EAF junction. The local radiation is separated from the initial arrivals by about 40 second due to the delayed triggering of the southern rupture. Out of the 22 southern stations, 19 recorded the complete rupture front radiation as it propagates southward (Figure 2a). Due to the proximity of these stations to the fault, the strong pulse comprises P, S, and surface waves, as the travel time differences between these phases are comparable to the source process duration. These 19 near-fault records offer a valuable opportunity to investigate the high-frequency radiation mechanisms of the Mw 7.8 earthquake.

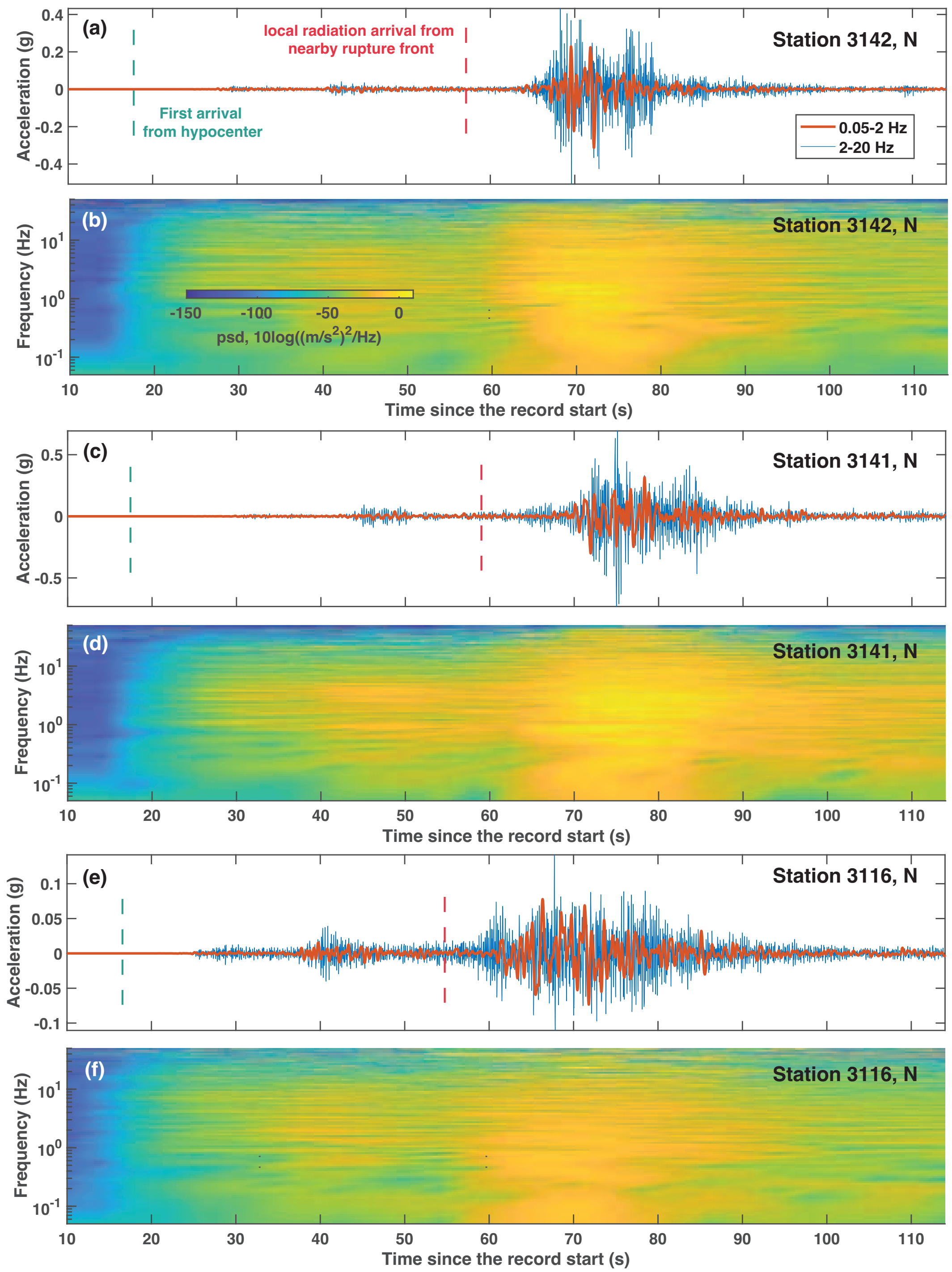

Figure 3. **(a), (c), (e)** North-south component accelerograms of Station 3142, 3141, and 3116, filtered in 0.05-2 Hz (red) and 2-20 Hz (blue). The green vertical line denotes the arrival of radiation from the rupture front near the station, as suggested by the spectrogram. **(b), (d), (f)** North-south component acceleration spectrogram of Station 3142, 3141, and 3116.

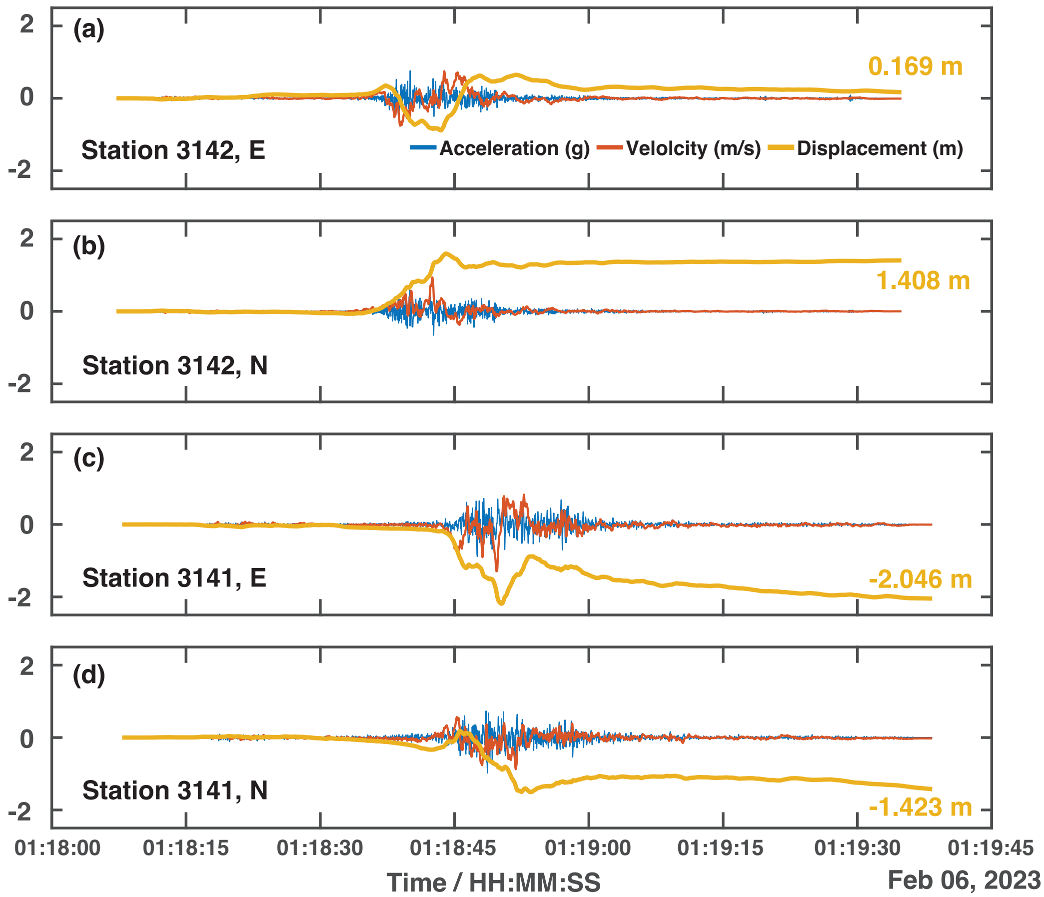

Figure 4. **(a)-(d)** Unfiltered seismograms after the local radiation from the nearby rupture arrives for Station 3142 east-west component, Station 3142 north-south component, Station 3141 east-west component, and Station 3141 north-south component, respectively. Blue lines are acceleration seismograms in units of earth gravity ($9.8\,\mathrm{m/s^2}$). Red lines are velocity seismograms in units of m/s. Yellow lines are displacement seismograms in units of meters. Yellow numbers indicate displacement values at the end of the records.

The local radiation from the nearby rupture, recorded by the 19 stations, contains energy across a wide range of frequencies. Figure 3 shows the acceleration records and spectrograms from the north-south component of three stations as examples: 3142, 3141, and 3116. High- and low-frequency radiation from the nearby rupture arrived simultaneously at these stations. The local radiation consists of a pulse with a finite duration of about 30 seconds, and the durations of the high- and low-frequency components are comparable. We inspected the other 16 stations and found the same characteristics. These results suggest that the high-frequency radiation likely originated from the rupture front, rather than from scattering sources away from the fault or significantly behind the rupture front. Similar observations have also been made in S. Yao and Yang (2025).

Due to their proximity to the fault, near-field stations experience static displacements by the end of the earthquake (e.g., Housner & Trifunac, 1967; Madariaga et al., 2019; J. Liu et al., 2024). We obtained the horizontal displacement time series of Stations 3141 and 3142 by double integrating the acceleration records Figure 4a-4d. Their final displacements are consistent with the left-lateral strike-slip mechanism of the earthquake (Figure 2b), suggesting the displacement time series can be treated as proxies for slip history. Notably, most high-amplitude acceleration and velocity motions occur during the slip-rise time. This again suggests the recorded high-frequency radiation is generated simultaneously as slip accelerates at the rupture front.

3 Loss of Horizontal Polarity at High-frequencies

Horizontal polarities of near-field ground motion provide valuable insights into rupture dynamics. It has been suggested that on a strike-slip fault, the FN ground velocity can be either greater or smaller than the FP ground velocity, depending on whether the rupture speed is sub-shear or super-shear. This phenomenon has been supported by observational studies (e.g., Somerville et al., 1997; Dunham & Archuleta, 2004; Graves & Pitarka, 2016; Abdelmeguid et al., 2023; Ben-Zion et al., 2024), theoretical studies (e.g., Dunham & Archuleta, 2005; Mello et al., 2016; Hu et al., 2019; Ben-Zion et al., 2024), and laboratory experiments (e.g., Mello et al., 2016; Rubino et al., 2020). Such horizontal polarity is attributed to both double-couple radiation patterns and rupture directivity.

We rotated the horizontal records of the 19 stations into FN and FP components, assuming an overall fault azimuth of 23° to the north based on surface rupture observations (Reitman, Briggs, Barnhart, Hatem, et al., 2023). We then windowed the local rupture radiation and calculated velocity spectrum ratios between the FN and FP components. We inspected the FN to FP ratio for all 19 stations (Figure 5a-5c, Figure S1-S7). At low frequencies, 16 of the 19 stations show a FN component greater than the FP component (Figure 5a). This is consistent with the overall sub-shear rupture, as constrained by the timing of rupture front arrivals (Abdelmeguid et al., 2023; Ren et al., 2024; Palo & Zollo, 2024; S. Yao & Yang, 2025) (Figure 2a). Three of the 19 stations show a FN component smaller than the FP component at low frequencies (Figure 5b), likely due to a small portion of supershear rupture (Abdelmeguid et al., 2023) or the fault bend near these stations (S. Yao & Yang, 2025). At the lowest frequency, the polarity often reverses, likely due to differences in polarity between static displacement and S-wave radiation.

Above a transition frequency, we observed a loss of horizontal polarity among these 19 very close stations (Figure 5c). The loss of horizontal polarity can be observed in both the 16 stations where FN is greater than the FP component (Figure 5a), as well as in the 3 stations where FN is smaller than the FP component (Figure 5b). We averaged the logarithm (base 10) of the individual spectra. The average ratio of all 19 stations shows a transition frequency between 0.3-0.4 Hz (Figure 5c). This value is lower than the commonly accepted rule-of-thumb value of 1 Hz that separates low- and high-frequency ra-

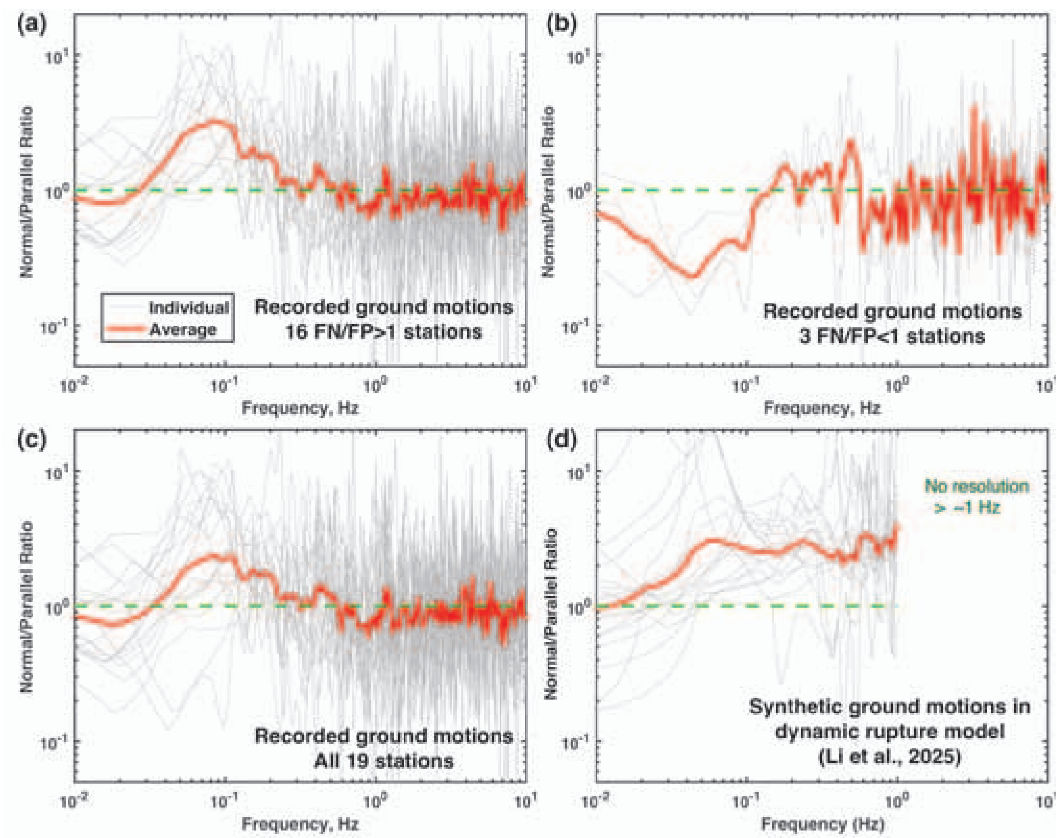

Figure 5. **(a)** The spectrum ratio between the FP and FN velocity seismograms is shown for the 16 southern stations that recorded the complete rupture front radiation and with FN greater than FP component at low frequencies: 2712, 8002, 2718, 3143, 3137, 3145, 3139, 3142, 3141, 3124, 3125, 3123, 3132, 3126, 3131, 3129. Gray lines are the spectrum ratio for each of the individual stations, while the red line represents the average spectrum ratio, obtained by averaging the logarithm (base 10) of the individual spectra. **(b)** Same as (a), but for the 3 of 19 stations with FN smaller than FP component at low frequencies: 3138, 3144, 3116. **(c)** Same as (a), all the 19 stations that recorded the complete rupture front radiation. **(d)** Same as (a), except that ground motions are synthetic data from the dynamic rupture model in B. Li et al. (2025). We included 16 out of 22 station locations that are within 10 km of the surface rupture: 2712, 2709, 8002, 2718, 2707, 3143, 3138, 3144, 3145, 3139, 3116, 3142, 3146, 3124, 3123, 3132. Other stations were not included because there are no collocated nodes in the numerical mesh. Results above ~ 1 Hz are not plotted because the numerical simulation has no resolution above ~ 1 Hz.

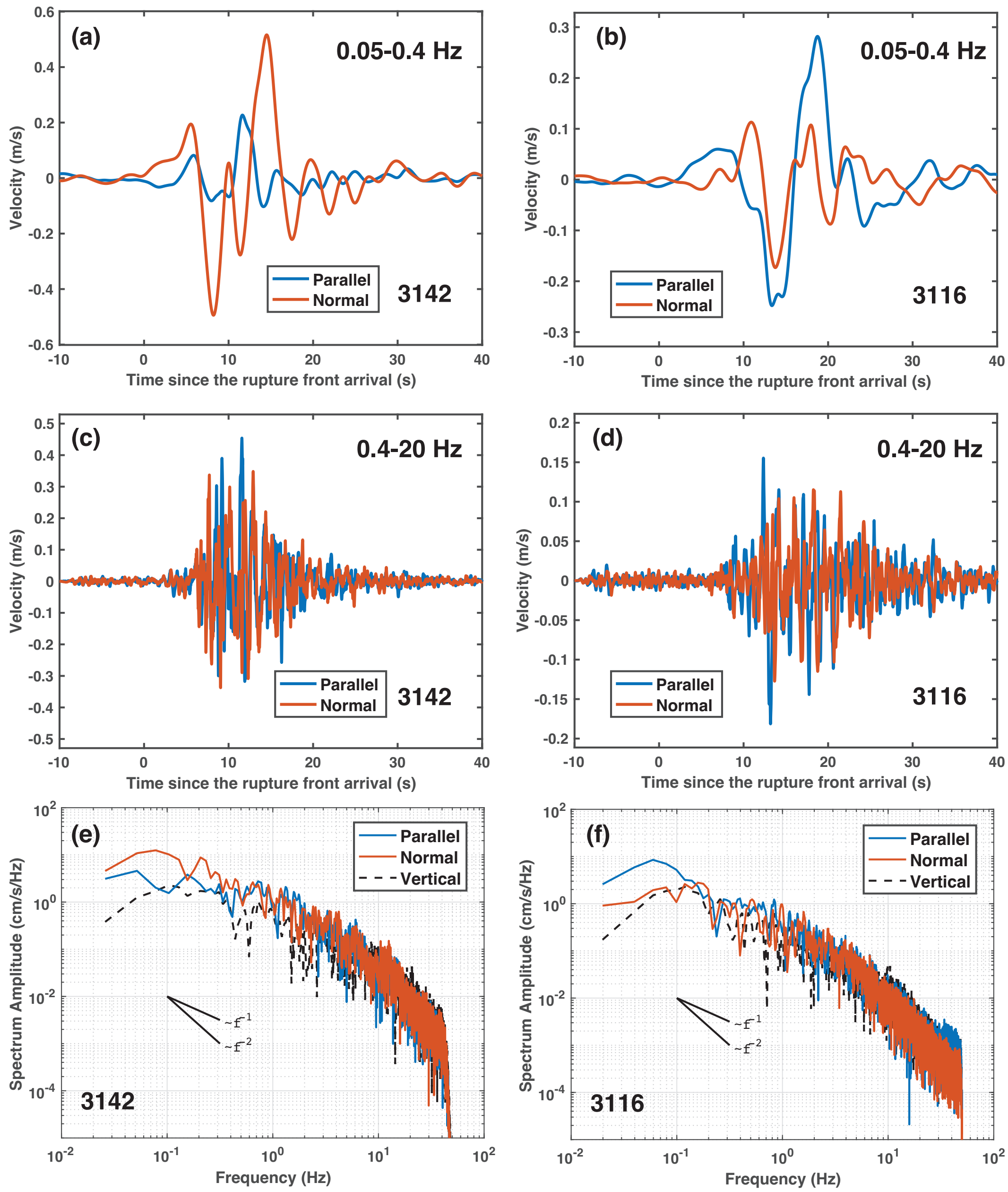

Figure 6. **(a), (b)** Comparison of the FP and FN velocity seismograms for Station 3142 and 3116, assuming a fault azimuth of 23° based on the overall trend of the surface rupture. Only the strong pulse after the rupture front arrival was analyzed. Windows are manually picked. The seismograms were filtered in the 0.05-0.4 Hz band. Station 3142 shows a FN component greater than the FP component, while Station 3116 shows a FN component smaller than the FP component. **(c), (d)** Same as (a) and (b), except that the seismograms are filtered in the 0.4-20 Hz band. For both stations, FN and FP components have comparable amplitude. **(e), (f)** Spectra of FP (blue solid line), FN (red solid line), and vertical (black dashed line) components for Station 3142 and 3116. Horizontal polarities are lost at high frequencies.

diation. A lower-than-expected transition frequency has also been reported for other earthquakes (Frankel, 2009; Graves & Pitarka, 2016; Ben-Zion et al., 2024).

As examples for the two station categories that exhibit different low-frequency polarity, we show the velocity seismograms and spectra of stations 3142 and 3116, respectively (Figure 6). When filtered in the 0.05-0.4 Hz band, one of the components has greater amplitude than the other (Figure 6a, 6b); however, FN and FP velocity amplitudes are about the same when filtered in the 0.4-20 Hz band (Figure 6c, 6d). A clear difference in spectrum level between the horizontal components can be seen below the transition frequency, while above that frequency, the two horizontal components have comparable spectrum levels (Figure 6e, 6f). Apparently, the high-frequency radiation from the rupture front does not retain the double-radiation pattern like its low-frequency counterpart.

4 Loss of Between-Horizontal-Component Correlations at High-frequencies

Theoretically, the amplitudes of the two components from a single seismic phase differ only by a fixed ratio, depending on the radiation pattern. In this case, no matter how complex the source time function is, the correlation coefficient between the time series of the two components would remain high. For the near-field records of the Mw 7.8 strike-slip rupture, we may assume that the two horizontal components of the rupture front radiation are dominated by S waves. If the source mechanism is coherent within the rupture front, the correlation coefficient between the two horizontal components should be high.

We calculated the correlation coefficients between the north-south and east-west component acceleration seismograms for the 19 near-fault stations that recorded the complete rupture front radiation. The correlation coefficient (CC) is calculated as the ratio between the covariance of the two time series and the product of their standard deviations,

$$\mathrm{CC} = \frac{\sum_{i=1}^{n}(a_i^{\mathrm{NS}} - \overline{a^{\mathrm{NS}}})(a_i^{\mathrm{EW}} - \overline{a^{\mathrm{EW}}})}{\sqrt{\sum_{i=1}^{n}(a_i^{\mathrm{NS}} - \overline{a^{\mathrm{NS}}})^2}\sqrt{\sum_{i=1}^{n}(a_i^{\mathrm{EW}} - \overline{a^{\mathrm{EW}}})^2}}, \tag{1}$$

where a^{NS} and a^{EW} are discrete acceleration records of the north-south and east-west component; $\overline{a^{\mathrm{NS}}}$ and $\overline{a^{\mathrm{EW}}}$ are the corresponding sample mean. n is the sampling number of the time series.

We slice the time series to analyze only the rupture front radiation. We apply different bandpass filters to the records, with the frequency band progressing from low to high. The frequency band center interval and bandwidth are 0.2 and 1, respectively, in logarithmic (base 10) space. CC is calculated for each moving filter. If the CC at the lowest frequency band is negative, we multiply all the CC values for that station by -1.

The CC between the two horizontal components is high at low frequencies, as shown in the examples of Station 3142 and 3116 (Figure 7a, 7b). We investigated all 19 stations and found the same characteristics (Figure 7c, Figure S8-S11). Low-frequency radiation reflects source properties averaged over long wavelengths. Therefore, a high CC value at low frequencies indicates that the source mechanism, averaged over a long distance, is coherent, which, as expected, corresponds to the sudden slip acceleration and deceleration of the rupture front. This result suggests that the assumption of a single dominant seismic phase is reasonable for low-frequency radiation.

As frequency increases, the CC drops significantly to near zero (Figure 7a-7c, S8-S11). This suggests that the source mechanism is no longer coherent when averaged over a short distance. Multiple seismic phases radiated from different rupture locations arrive at the station at the same time, and they may have drastically different amplitudes

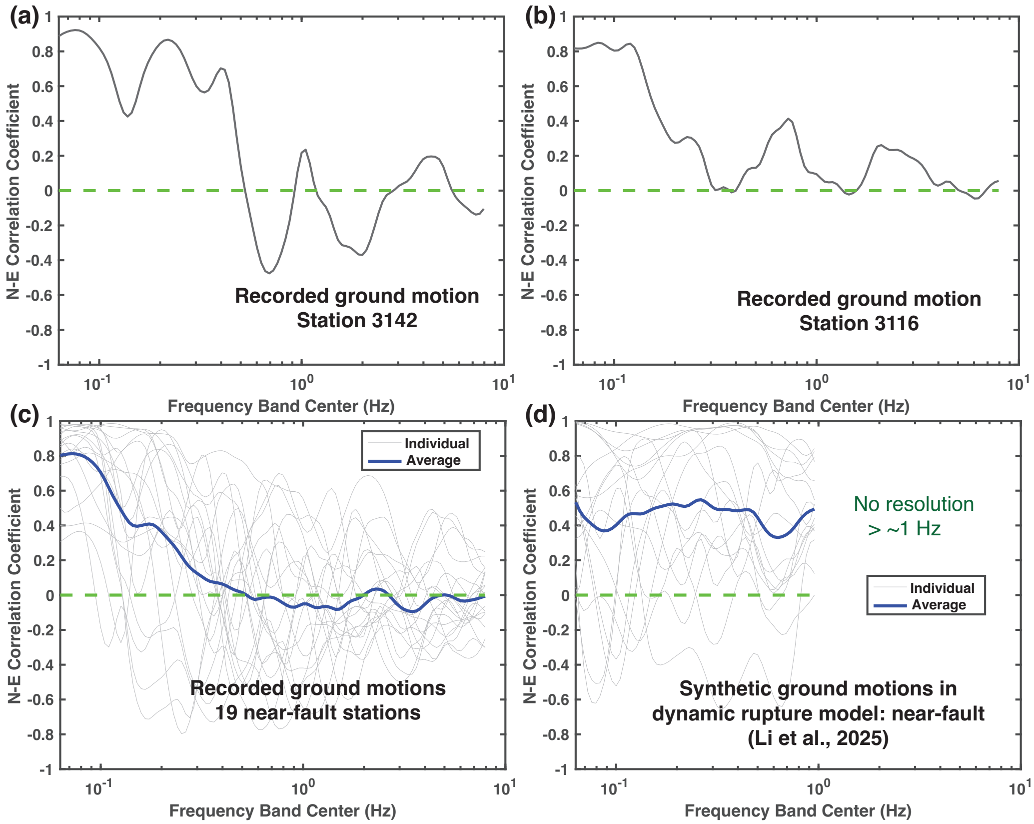

Figure 7. **(a), (b)** Correlation coefficient (CC) between north- and east-component acceleration filtered in a moving frequency band for Station 3142 and 3116. Only the strong pulse after the rupture front arrival was analyzed. The frequency band center interval and bandwidth are 0.2 and 1, respectively, in logarithmic (base 10) space. Green dashed lines denote the zero CC level. **(c)** The same as (a) and (b) but plot the individual CC for the 19 near-fault stations (gray lines) and the average CC (blue line). **(d)** Similar to (c), except the data are synthetic ground motions within 10 km of the fault from the dynamic rupture model in B. Li et al. (2025). We included 16 out of 22 station locations that are within 10 km of the surface rupture: 2712, 2709, 8002, 2718, 2707, 3143, 3138, 3144, 3145, 3139, 3116, 3142, 3146, 3124, 3123, 3132. Other stations were not included because there are no collocated nodes in the numerical mesh. Results above $\sim$ 1 Hz are not plotted because the numerical simulation has no resolution above $\sim$ 1 Hz.

or radiation patterns. As a result, high-frequency radiation becomes incoherent, even for the two horizontal components at the same station.

The transition frequency between high and low CC values varies among stations; sometimes, it is even hard to define (Figure 7a, 7b, S8-S11). However, the average frequency-dependent CC of all 19 stations shows a well-defined transition: CC is as high as 0.8 at the lowest frequency, drops to zero at $\sim$ 0.4 Hz, and remains zero for higher frequencies (Figure 7c). Notably, this transition frequency of $\sim$ 0.4 Hz is almost the same as the frequency at which the horizontal polarity is lost for these 19 stations. This suggests that an incoherent source mechanism within the rupture front is likely also responsible for causing the loss of horizontal polarity at high frequencies, in addition to causing the low CC value. The 0.4 Hz transition frequency is lower than the commonly accepted rule-of-thumb value of 1 Hz that separates low- and high-frequency radiation. Assuming a characteristic wave speed of 2-4 km/s, the observed 0.4 Hz transition frequency corresponds to a transition complexity wavelength of 5-10 km.

5 Discussion

5.1 High-frequency Radiation Mechanisms

The difficulty in modeling higher-frequency ground motion reflects our limited knowledge of the small-scale complexities in the source process and along the wave propagation path (Aki, 2003). The issue likely concerns not only how to better invert parameters for a specific model that describes small-scale complexities but also which model is more appropriate for capturing these complexities. Our observation of the loss of polarity and coherence at $\sim$ 0.4 Hz, along with other observational studies of the 2023 Mw 7.8 Kahramanmaraş earthquake, may provide constraints that help distinguish high-frequency radiation mechanisms. Here, we summarize six types of high-frequency radiation mechanisms proposed within the scientific community and discuss their applicability in explaining the observed high-frequency characteristics of the Mw 7.8 earthquake.

5.1.1 Heterogeneous parameters on a planar fault

The arguably most common parameterization is incorporating heterogeneous rupture kinematics on a planar fault, such as slip amplitude and rupture timing, which may arise from inhomogeneous mechanical properties, such as stress fields, rock types, and friction (Figure 8a) (e.g., Madariaga, 1977; Achenbach & Harris, 1978; Andrews, 1981; Papageorgiou & Aki, 1983a, 1983b; Spudich & Frazer, 1984; Bernard & Madariaga, 1984; Graves & Pitarka, 2010; Baumann & Dalguer, 2014; Andrews & Ma, 2016). An equivalent parameterization is to populate many subevents on a planar fault, which have similar focal mechanisms as the main fault. The subevents rupture at different times and have various sizes, following certain magnitude-frequency distributions (e.g., Gutenberg-Ricter Law) (e.g., Hanks, 1979; Boatwright, 1982, 1988; Frankel, 1991, 1995; Zeng et al., 1994, 1995; Zeng & Anderson, 1996). Such planar-heterogeneity parameterization can successfully reproduce the stochastic characteristics of high-frequency radiation, and it is arguably a primary conceptualization in discussing fault complexity (e.g., Lay et al., 2012).

However, the planar-heterogeneity parameterization might not explain the observed loss of horizontal polarity at high frequencies (Figure 5a, 5c). Graves and Pitarka (2016) investigated the near-fault records of the 1979 Mw 6.5 Imperial Valley earthquake. They found that kinematic models with heterogeneous slip, rupture speed, and rise time may slightly lower the FN/FP ratio compared to homogeneous models, due to reduced signal coherence. However, the planar-heterogeneity models cannot reproduce the FN/FP ratio approaching unity at high frequencies. This is because the fault is planar, and the FN motion still has more potential to constructively interfere than the FP motion. Sim-

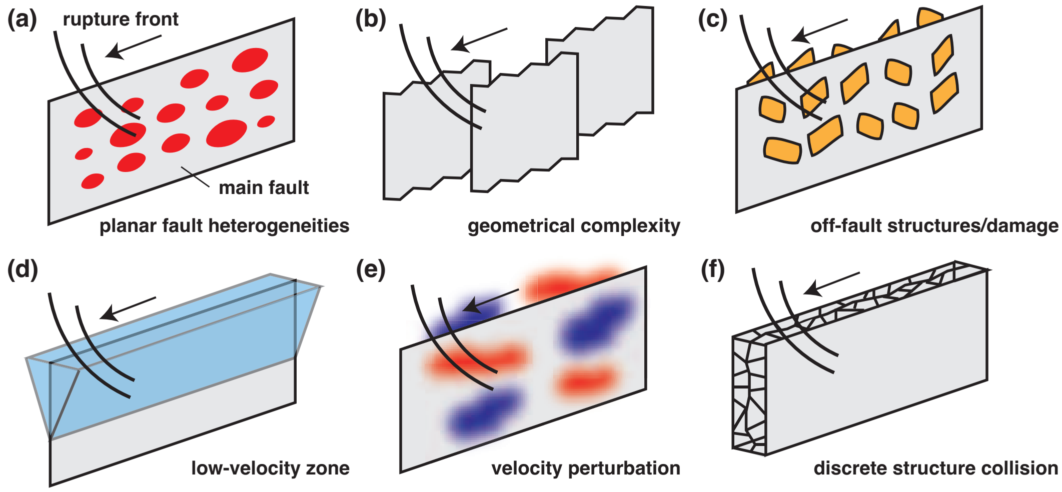

Figure 8. Schematics of different proposed mechanisms for high-frequency generation: **(a)** Heterogeneous stress and slip on a planar fault. **(b)** Complexities in fault geometry, including smaller-scale roughness and larger-scale fault bend and stepovers. **(c)** Off-fault structures created or triggered to slip during dynamic ruptures. **(d)** Trapped waves in the low-velocity fault damage zone disturb the radiation. **(e)** Patchy anomalies in the near-fault velocity structure scatter the wavefield. **(f)** Elastic impact and collision of discrete structures in the fault zone. References for these proposed mechanisms are provided in Section 5.1

ilar to the 1979 Mw 6.5 Imperial Valley earthquake, the near-fault stations of the 2023 Mw 7.8 Kahramanmaraş earthquake also show no horizontal polarity at high frequencies (Figure 5c). Therefore, we suspect that the planar-heterogeneity mechanism might not be sufficient to model the observed loss of radiation polarity at high frequencies in the 2023 Mw 7.8 Kahramanmaraş earthquake.

5.1.2 Complex fault geometry

Complex fault geometry can perturbate the rupture process and generate high-frequency radiation (Figure 8b), such as small-scale roughness (e.g., Dunham et al., 2011; Shi & Day, 2013; Mai et al., 2018; Withers, Olsen, Day, & Shi, 2018; Withers, Olsen, Shi, & Day, 2018; Taufiqurrahman et al., 2022; Vyas et al., 2023) and large-scale fault bend and stepovers (e.g., Adda-Bedia & Madariaga, 2008; Hu et al., 2018; Lozos et al., 2025). Variation in fault geometry can cause heterogeneous radiation patterns, leading to a lower FN/FP ratio compared to a planar fault model.

Assuming a characteristic wave speed of 2-4 km/s, the observed $\sim$ 0.4 Hz transition frequency corresponds to a transition complexity wavelength of 5-10 km. Substantial variation in the main fault surface rupture at such a long wavelength has not been observed (Reitman, Briggs, Barnhart, Hatem, et al., 2023; J. Meng et al., 2024; Provost et al., 2024). Notably, Graves and Pitarka (2016) showed that the FN/FP ratio at high frequencies cannot be reduced to around unity with a reasonable roughness configuration for the 1979 Mw 6.5 Imperial Valley earthquake. These results lead us to suspect that geometrical complexity may not be the key factor in causing the $\sim$ 0.4 Hz transition frequency observed in the 2023 Mw 7.8 Kahramanmaraş earthquake, although more quantitative models are needed to test this hypothesis.

5.1.3 Dynamic triggering of off-fault structures

Another popular hypothesis for high-frequency radiation is considering off-fault structures triggered by the main rupture (Figure 8c). A conceptual model of this category is existing smaller faults dynamically triggered by the main rupture front. This idea can be extended from the subevent hypothesis of high-frequency radiation (e.g., Hanks, 1979; Boatwright, 1982, 1988; Frankel, 1991, 1995; Zeng et al., 1994, 1995; Zeng & Anderson, 1996), except that the subevents do not need to have the same focal mechanisms as the main rupture (Zeng et al., 1995), and that each subevent's slip does not need to equal the main fault's slip at the corresponding location (Frankel, 1995).

The seismicity around the EAF contains many normal faulting events, as suggested by both background seismicity (Güvercin et al., 2022) and the aftershocks of the Mw 7.8 Kahramanmaraş earthquake (Petersen et al., 2023; Güvercin, 2024; Wan et al., 2024; Ma et al., 2024; O. Tan, 2025). If many normal faults were dynamically triggered during the Mw 7.8 main rupture, the resulting ground motions would be the combination of main-fault strike-slip radiation and the sub-fault normal-slip radiation; in that case, a loss of polarity and coherence of the ground motions at high frequencies is expected. Considering a characteristic transition complexity wavelength of 5-10 km, the largest dynamically triggered events would have a magnitude of 5 to 6 (Wells & Coppersmith, 1994), consistent with the large normal faulting event magnitudes observed in the seismotectonic studies of EAF (Güvercin et al., 2022).

An alternative model is off-fault damage dynamically created by the main rupture front (e.g., Ben-Zion & Ampuero, 2009; Castro & Ben-Zion, 2013; Okubo et al., 2019; Ben-Zion et al., 2024). The dynamic strain induced by the rupture front can be large enough to damage the nearby medium. The creation of damage simultaneously radiates seismic energy, adding to the original wave fields. The damage radiation could be different from the main rupture radiation (e.g., Ben-Zion & Ampuero, 2009). As a result, the total radiation would lose polarity and coherence at higher frequencies when the radiation wavelength is comparable to or smaller than the damage size.

If the off-fault damage model were responsible for the Mw 7.8 Kahramanmaraş earthquake, we might predict a 5-10 km coseismic damage based on the ~ 0.4 Hz transition frequency, which has not yet been reported by field observations, to the best of our knowledge. Nevertheless, even if large coseismic damage is not observed, we cannot rule out that this mechanism affects the radiation at frequencies higher than the 0.4 Hz transition frequency. More modeling is needed to quantitatively test the off-fault damage mechanism for the Mw 7.8 earthquake, such as whether it can reproduce both the low- and high-frequency spectra without producing too much high-frequency energy, which is a known issue for other subevent-type models of high-frequency radiation (Frankel, 1995).

5.1.4 Low-velocity zone

Seismic wave speed within a few kilometers of a strike-slip fault is commonly found to be abnormally lower than the surrounding medium, which is generally believed to be created by repeated ruptures (e.g., Y.-G. Li et al., 1990, 1994; Vidale & Li, 2003; Ben-Zion et al., 2003; Y.-G. Li et al., 2004; Cochran et al., 2009). This near-fault structure is often referred to as a low-velocity zone, or fault damage zone. During co-seismic rupture, the low-velocity zone may trap and scatter the seismic energy emitted by the main rupture by reflection and refractions (e.g., Y.-G. Li & Vidale, 1996; Ben-Zion, 1998). The complex wavefield could further alter the dynamic rupture process, causing more complex seismic radiation (e.g., Harris & Day, 1997; Huang et al., 2014).

The low-velocity zone has been proposed as a key mechanism for high-frequency radiation (e.g., Takenaka et al., 2003; Graves & Pitarka, 2016) (Figure 8d). Takenaka et al. (2003) investigated the S wave radiation pattern from the aftershocks of the 1997

Northwestern Kagoshima, Japan, earthquakes, with magnitude ranging from 2.1 to 5.2. They found that the S wave radiation pattern becomes stochastic above 3.5 Hz. In particular, they found remarkable differences in radiation patterns above 3 Hz for 12 pairs of events that are very close to each other. Takenaka et al. (2003) hypothesized that the strong SH–SV mixing locally occurring around the sources, likely caused by the low-velocity zone, is responsible for stochastic radiation patterns at high-frequencies.

In addition, Graves and Pitarka (2016) found that incorporating a low-velocity zone has a strong impact on the near-fault FN/FP ratio at high frequencies. Their kinematic model with fault roughness and stochastic rupture parameters cannot reproduce the observed FN/FP ratio around unity in the 1979 Mw 6.5 Imperial earthquake. Adding a 5 km deep low-velocity zone with stochastic perturbation of velocity can significantly reduce the model's FN/FP ratios at high frequencies by 30%, making them close to the observed level. Graves and Pitarka (2016) hypothesized that this is due to the multipathing and scattering of shorter wavelength energy within the low-velocity zone.

To the best of our knowledge, no direct evidence has been reported of a low-velocity zone around the 2023 Mw 7.8 Kahramanmaraş earthquake rupture. However, a low-velocity zone around the East Anatolian Fault likely exists, considering its common occurrence in strike-slip fault systems, including the nearby North Anatolian Fault (Ben-Zion et al., 2003). There is some indirect evidence for a low-velocity zone. One is the extensive off-fault damage around the Mw 7.8 earthquake surface ruptures (J. Liu et al., 2025). Another piece of indirect evidence is the discrepancy between shallow slip and slip at intermediate depths, commonly referred to as the shallow slip deficit. Studies have suggested a correlation between shallow slip deficit and the existence of low-velocity zones (e.g., Fialko et al., 2005; X. Xu et al., 2020; Antoine et al., 2024). Coseismic slip inversion of the Mw 7.8 earthquake indicates a shallow slip deficit (Barbot et al., 2023; Tong et al., 2023; Jia et al., 2023; L. Xu et al., 2023; W. Wang et al., 2023; Y. Zhang et al., 2023; J. Liu et al., 2024; T. Kobayashi et al., 2024; K. Wang et al., 2024), suggesting a possible low-velocity fault zone. Future rupture models of the 2023 Mw 7.8 Kahramanmaraş earthquake should incorporate a low-velocity zone and test whether the observed high-frequency radiation characteristics can be reproduced.

5.1.5 Patchy anomalies in the near-fault velocity structure

Seismic wave scattering by small-scale velocity anomalies has long been recognized as an important mechanism for high-frequency radiation (e.g., Sato et al., 2012; Shearer, 2015). While wave scattering is typically categorized as a path effect, Imperatori and Mai (2012) showed through numerical models that patchy anomalies in the near-fault velocity structure can generate stochastic high-frequency radiation, even at very close stations (Figure 8e). By modeling the high-frequency attenuation structure in Southern California using scattering theory, Lin and Jordan (2023) suggested that crustal velocity heterogeneities have a characteristic outer scale of 8 km. Interestingly, this scale aligns with the 5-10 km transition wavelength suggested by the 0.4 Hz transition frequency observed in the 2023 Mw 7.8 Kahramanmaraş earthquake. Future numerical simulations may offer a more quantitative test for this hypothesis.

5.1.6 Elastic impact and collision of discrete structures in the fault zone

Recently, a hypothesis has been proposed suggesting that elastic impacts among fault zone structures play a key role in generating high-frequency radiation (Tsai & Hirth, 2020; Tsai et al., 2021). This idea is inspired by geological observations showing that fault zones often contain complex structures, such as granular fault gouges and interconnected fracture networks (e.g., Chester & Chester, 1998; Faulkner et al., 2003; Swanson, 2006). During coseismic rupture, these structures may lose frictional contact and impact each other, accommodating large-scale fault motion in the presence of small-scale geometric incompatibilities (Figure 8f). The radiation produced by these elastic impacts is of higher frequency than that from large-scale slip motion, due to the short timescale of the impacts.

The elastic impact model may help explain the observed loss of radiation polarity and coherence at high frequencies, as indicated by first-order analysis with simplified theoretical models (Tsai & Hirth, 2020; Tsai et al., 2021). However, it is not immediately obvious whether the elastic impact model can reproduce the transition frequency of 0.4 Hz in the 2023 Mw 7.8 Kahramanmaraş earthquake with reasonable parameters. Future research is needed to develop a parameterization scheme that simultaneously incorporates elastic impacts and large-scale rupture dynamics within the same rupture model. This approach would allow for a quantitative test of whether the elastic impact mechanism is consistent with multiple lines of evidence, such as mapped fault zone structures, the transition frequency between low- and high-frequency radiation, and the scaling between low- and high-frequency spectra.

5.2 Source Contribution to High-frequency Radiation in Relation to Path Scattering

Scattering from complex structures along the wave path, such as heterogeneous velocity structures and irregular ground topography, has long been recognized as a primary mechanism determining the stochastic high-frequency radiation characteristics away from the source (e.g., Takemura et al., 2009; Sato et al., 2012; Takemura et al., 2015; Shearer, 2015). In the following section, we discuss the source contribution to high-frequency radiation in relation to the scattering effects at various distances for the 2023 Mw 7.8 Kahramanmaraş earthquake.

5.2.1 *Near fault (<10 km)*

Our analysis shows that the stochastic characteristics exist above 0.4 Hz for the stations within 10 km of the Mw 7.8 rupture (Figure 3c, 4a). At these stations, high-frequency waves from near-fault might have only traveled a few wavelengths, and they arrive simultaneously with the polarized low-frequency radiation (rather than being coda). It suggests that the dominant mechanisms for the stochastic high-frequency characteristics are likely to occur on or near the fault. It is still possible that near-fault scattering structures, such as patchy seismic velocity perturbation, cause the observed stochastic characteristics (Imperatori & Mai, 2012), but the cause is unlikely the seismic velocity perturbation away from the fault.

5.2.2 *Regional distance (10-190 km)*

At a regional distance, the scattering effect becomes significant for high-frequency radiation. However, there might still be imprints of the source in the high-frequency characteristics. We test this hypothesis by investigating 60 stations that are beyond 10 km of the Mw 7.8 rupture and recorded the Mw 7.8 radiation with a signal-to-noise ratio greater than 10 (Table S1). The most distant selected station is 190 km away from the fault. It is challenging to perform frequency-dependent polarity analysis as in Section 3 because the theoretical polarity at low frequency is strongly affected by the finite fault effect. Nevertheless, we can still perform the frequency-dependent coherence analysis as in Section 4, since we do not need to assume a polarity direction to calculate correlation coefficients.

For simplicity, we do not window the records of these 60 stations, and the records contain the whole event radiation. The results are shown in Figure 9a. The individual frequency-dependent correlation coefficient curves for the 60 regional stations show notable variation, likely due to specific crustal scattering along individual ray paths. How-

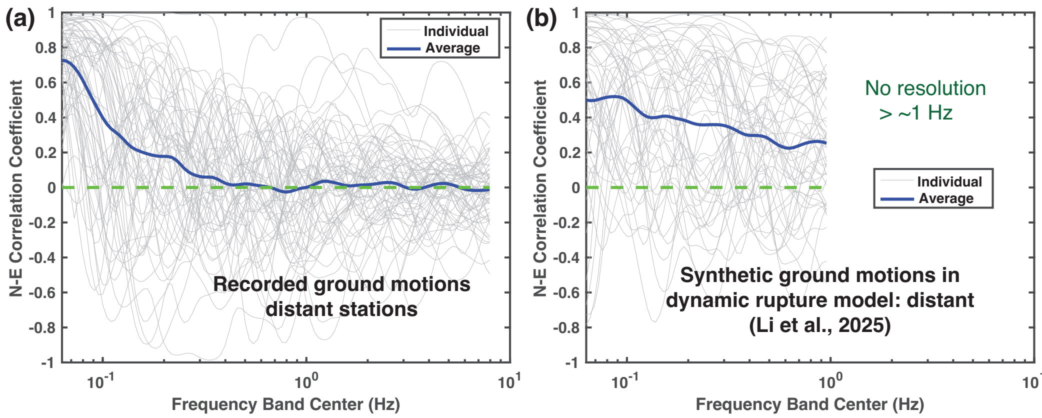

Figure 9. **(a)** Correlation coefficient between north- and east-component acceleration filtered in a moving frequency band for 60 regional stations more than 10 km away from the fault and with a signal-to-noise ratio greater than 10 (grey triangles in Figure 1a). The whole record is used for these 60 stations. The frequency band center interval and bandwidth are 0.2 and 1, respectively, in logarithmic (base 10) space. Gray lines represent the correlation coefficients of individual stations, and the blue line represents the average. **(b)** Similar to (a), except the data are synthetic ground motions more than 10 km away from the fault from the dynamic rupture model in B. Li et al. (2025). We included data from 48 out of the 60 station locations in (c); 12 stations were not included because there are no collocated nodes in the numerical mesh. The name and location of these regional stations can be found in Table S1.

ever, the stacked frequency-dependent correlation coefficient exhibits the same transition behavior as the stacked correlation coefficient of the 19 stations within 10 km of the fault (Figure 7c), with the transition frequency also occurring at ~ 0.4 Hz. The stacked frequency-dependent correlation coefficient reflects a common factor across all the records, which is the source. This suggests that the high-frequency radiation characteristics near the rupture front are preserved as the waves propagate over regional distances.

Many studies have reported frequency-dependent radiation patterns for earthquakes with moderate magnitudes (M2-5) (e.g., Satoh, 2002; Takenaka et al., 2003; Castro et al., 2006; Takemura et al., 2009; M. Kobayashi et al., 2015; Kotha et al., 2019; Trugman et al., 2021). Among these, two studies have suggested that high-frequency radiation at distant stations retains near-fault characteristics. Takenaka et al. (2003) observed distortion in the S-wave radiation pattern above 3.5 Hz at hypocentral distances of 12-20 km for aftershocks of the 1997 Northwestern Kagoshima, Japan, earthquakes. Notably, 12 pairs of events less than 500 meters apart exhibited significant differences in high-frequency radiation, suggesting a near-fault origin for these stochastic characteristics. Trugman et al. (2021) found that the P-wave radiation pattern becomes isotropic for small earthquakes in Oklahoma, United States. They observed no systematic trends in the residuals or wavefield fits as a function of hypocentral distance, from ~ 3 to 35 km, implying that high-frequency characteristics bear the imprint of the source. Future studies could investigate the high-frequency characteristics of small earthquakes near the East Anatolian Fault, though this lies beyond the scope of the current study.

5.2.3 Teleseismic distance

At teleseismic distances, recorded radiation originates from the downgoing waves generated by the source. These waves travel into the deep Earth and reach the stations

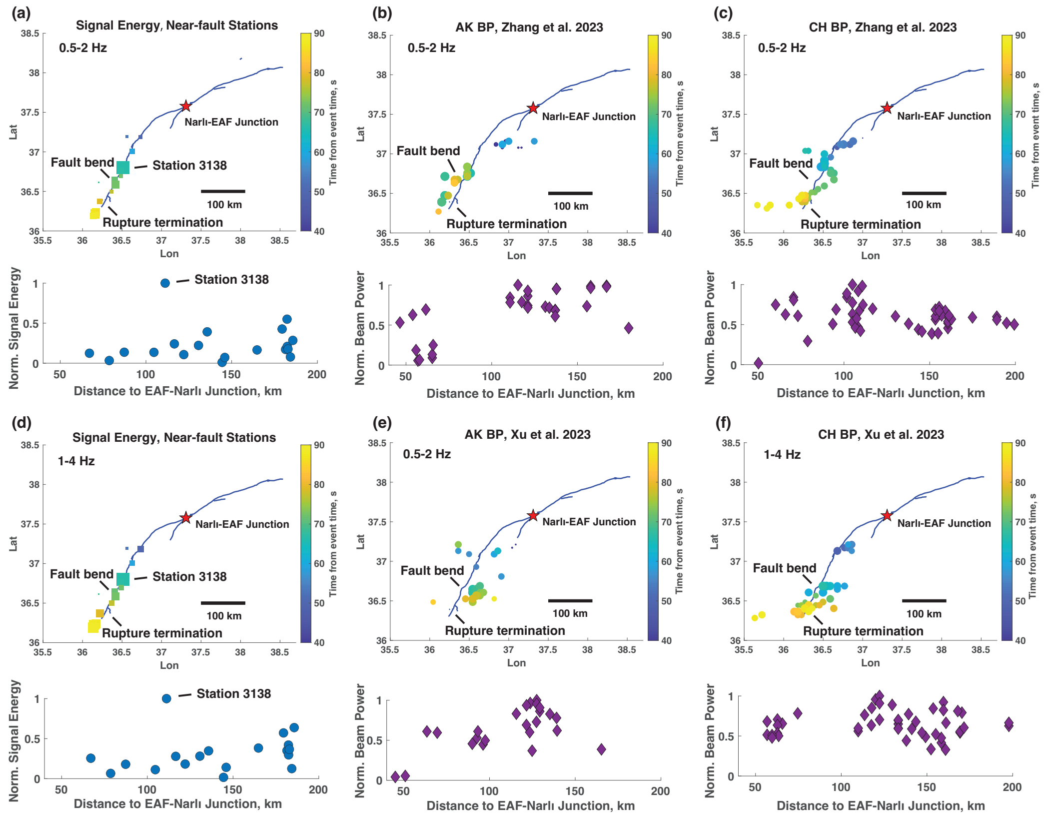

Figure 10. **(a), (d)** Total signal energy in (a) 0.5-2 Hz and (d) 1-4 Hz for the three-component velocity seismograms from near-fault stations (details in text). The top panels show the spatial distribution of the stations, where color indicates the arrival time of the radiation signal and size represents the normalized amplitude of the signal energy. The bottom panels display the total signal energy normalized by the maximum value as a function of the distance from the stations to the Narlı-EAF junction (blue dots). **(b), (c), (e), (f)** Back-projection beam power reported by two studies using two regional arrays: (b) Y. Zhang et al. (2023), Alaska (AK) array, 0.5-2 Hz; (c) Y. Zhang et al. (2023), China (CH) array, 0.5-2 Hz; (e) L. Xu et al. (2023), Alaska (AK) array, 0.5-2 Hz; (f) L. Xu et al. (2023), China (CH) array, 1-4 Hz. The top panels show the spatial distribution of radiators identified by back-projection along the southern rupture, selected based on conditions of being south of the event hypocenter and occurring within 90 seconds of the event start time. The color represents the time of the radiators, and the size corresponds to the normalized amplitude of the beam power. The surface rupture (blue lines) were obtained from the `simple_fault` files within the fault rupture mapping dataset provided by Reitman, Briggs, Barnhart, Thompson Jobe, et al. (2023). The bottom panels show the beam power normalized by the maximum value as a function of distance from the radiators to the Narlı-EAF junction (purple diamonds).

from below at a steep angle. Double-couple type source models, such as a finite-fault model and a multi-point source model, may explain the waveforms up to a particular frequency (e.g., Ye et al., 2016; Yue & Lay, 2020). However, at higher frequencies, teleseismic waveforms become more complex and usually cannot be modeled deterministically. Because teleseismic radiation might be strongly altered by scattering and attenuation along the ray path, it is challenging to distinguish whether the high-frequency complexity originates from the source or path.

Nevertheless, the high-frequency radiation sources at different times during a rupture can be located by utilizing arrival time move-outs at different teleseismic stations, using methods such as back-projection (e.g., Ishii et al., 2005; Krüger & Ohrnberger, 2005; Y. Xu et al., 2009; H. Zhang & Ge, 2010; Kiser & Ishii, 2011; Koper et al., 2011; H. Yao et al., 2011; L. Meng et al., 2012; Fan & Shearer, 2015; Yagi & Okuwaki, 2015; Yin et al., 2016; D. Wang et al., 2016; B. Li & Ghosh, 2017; Bao et al., 2019; F. Tan et al., 2019; Bao et al., 2022; Yue et al., 2022; Wei et al., 2022; Vera et al., 2024). It is commonly found that these high-frequency radiators are located near the fault identified by other datasets, and their trajectory seemingly tracks the rupture propagation process. Therefore, teleseismic high-frequency waveforms are often considered to still contain meaningful information about the radiation source, even though the exact physical meaning is uncertain (B. Li et al., 2022).

Several back-projection analyses have been published for the 2023 Mw 7.8 Kahramanmaraş earthquake (Y. Zhang et al., 2023; L. Xu et al., 2023; Mai et al., 2023; Jia et al., 2023; Ding et al., 2023; Petersen et al., 2023; Wan et al., 2024). Here, we roughly estimated high-frequency radiation energy from the near-fault records and compared it with the back-projection results in Y. Zhang et al. (2023) and L. Xu et al. (2023), both of which employ a slowness-enhanced back-projection method (L. Meng et al., 2016) (Figure 10). We assume that the radiation recorded at the near-fault stations (Figure 2a) is not significantly affected by attenuation, and that the radiation energy from the nearby rupture can be approximated by the kinetic energy from ground motions. The kinetic energy is assumed to be proportional to the sum of the ground velocity squared at a station, which can be calculated as the sum of the signal power from the three-component velocity seismograms, windowed to include only rupture front radiation. Using Parseval's theorem, we can distribute the total signal energy across different frequencies and compare the signal energy in a specific frequency band with the back-projection beam power.

The radiation energy patterns estimated from near-fault records show similarities to the back-projection results. Station 3138 exhibits significant radiation energy, at least three times greater than any other station, in both the 0.5-2 Hz (Figure 10a) and 1-4 Hz (Figure 10d) bands. The above-average signal energy of Station 3138 is also reported by S. Yao and Yang (2025). The four back-projection analyses in Y. Zhang et al. (2023) and L. Xu et al. (2023) all identify high-frequency radiators with relatively larger beam power near Station 3138 (Figure 10b, 10c, 10e, 10f), located approximately 110 km from the Narlı-EAF junction. We hypothesize that the increased high-frequency radiation is related to the fault bend south of Station 3138, or to rupture speed variations between subshear and supershear rupture (Figure 2a). Additionally, stations south of the fault bend exhibit greater high-frequency radiation energy than those to the north, a pattern also observed in the back-projection results. This "south greater than north" trend contrasts with the coseismic static slip distribution, where the fault segment north of the bend experiences greater slip than the southern segment (e.g., Ma et al., 2024; S. Yao & Yang, 2025). The greater high-frequency radiation south of the fault bend might be associated with the complex fault structures near the rupture termination or the rupture directivity effect.

We note that the comparison presented above relies on several assumptions, and there are clear differences between the teleseismic back-projection results and the radiation energy estimated from the near-fault stations. The choice of processing procedures in specific back-projection methods may also play a role. We compared the radiation energy patterns estimated from near-fault records with those from three other back-projection studies that provided radiation energy estimates (Mai et al., 2023; Petersen et al., 2023; Wan et al., 2024). The aforementioned characteristics are not as clear in these studies (Figure S12, S13, S14). A more detailed comparison between the back-projection results and near-fault strong-motion records would be valuable in future studies, but it is beyond the scope of the present work.

In any case, the shared features observed between near-fault and teleseismic high-frequency radiation suggest that the high-frequency radiation source, regardless of its nature, may retain its characteristics at teleseismic distances, despite scattering and attenuation along the ray path. This result supports recent studies that propose using back-projection radiators to quickly assess near-fault seismic hazards after major earthquakes (e.g., Feng & Meng, 2018; Smith & Mooney, 2021; Chen et al., 2022, 2023).

5.3 Challenges in Modeling Realistic High-frequency Radiation

High-frequency ground motions of large earthquakes have been recognized as stochastic, of finite-duration, and band-limited (e.g., Housner, 1947; Hanks & McGuire, 1981). While the high-frequency spectrum amplitude may be predicted by classic models, the time series usually cannot be synthesized deterministically with a physical model (Hanks, 1979; McGuire & Hanks, 1980). Instead, the high-frequency ground motions are usually modeled empirically with stochastic Green's functions (e.g., Boore, 1983; Hartzell et al., 1999; Boore, 2003; Motazedian & Atkinson, 2005) or as a stochastic rupture process (e.g., Zeng et al., 1994; P. Liu et al., 2006; Gallovič & Brokešová, 2007; Graves & Pitarka, 2010; Withers, Olsen, Day, & Shi, 2018; Taufiqurrahman et al., 2022). Many simulations of broadband ground motions utilize a hybrid scheme, where low- and high-frequency waveforms are separately calculated by deterministic and stochastic models, respectively, and are combined together following specific rules (e.g., Kamae et al., 1998; P. Liu et al., 2006; Gallovič & Brokešová, 2007; Frankel, 2009; Pulido & Dalguer, 2009; Mai et al., 2010; Irikura & Miyake, 2011).

While current stochastic models have achieved significant success, they do not capture all the characteristics of high-frequency radiation. The transition boundary between low- and high-frequency simulations is typically set empirically (e.g., Hartzell et al., 1999) and considered constant across different earthquakes, which may misrepresent reality (Frankel, 2009; Ben-Zion et al., 2024). In fact, the observed transition boundary of ~ 0.4 Hz for the 2023 Mw 7.8 Kahramanmaraş earthquake is lower than the commonly accepted value of 1 Hz. A similar conclusion was reached by Čejka et al. (2023), who found that a transition boundary around 0.4 Hz is necessary for their hybrid broadband simulations to accurately reproduce the observed ground motions. Additionally, stochastic models may fail to capture changes in frequency content over time (Frankel, 1995) and may underestimate the degree of correlation between frequencies (e.g., Stafford, 2017; Bayless, 2018) and stations (e.g., Loth & Baker, 2013). Our results, along with other characterizations of the 2023 Kahramanmaraş earthquake's strong ground motions, could serve as valuable observational benchmarks for future studies aimed at improving the design of stochastic ground motion simulations.

Dynamic rupture models provide rupture scenarios and ground motions that physically coordinate stress conditions, fault geometries, friction and deformation rheology on and off the fault, as well as the elastic and inelastic response of the medium (e.g., Harris et al., 2018). As such, they can be used to simulate both low- and high-frequency radiation in a self-consistent manner. Several studies have developed dynamic rupture models for the 2023 Mw 7.8 Kahramanmaraş earthquake to explain the observed low-frequency ground motion characteristics (e.g., Z. Wang et al., 2023; Jia et al., 2023; Gabriel et al., 2023; Ding et al., 2023; He et al., 2024; B. Li et al., 2025). However, these models may not fully account for the observed 0.4 Hz transition between low- and high-frequency radiation, even though some are constrained by multiple datasets, including surface rupture, aftershock locations, coseismic deformation, the regional stress field, and 3D velocity structure. To illustrate this point, we apply polarity and correlation analyses to the synthetic ground motions from the dynamic rupture model in B. Li et al. (2025), which can numerically resolve ground motion up to 1 Hz, using the same methods and station locations as in Section 3 and Section 4. We did not observe a behavioral transition at 0.4 Hz in either the horizontal polarity (Figure 5d) or signal coherence (Figure 7b, 9b).

To reproduce realistic high-frequency ground motions with dynamic rupture models, it is generally believed that some stochastic source representations or parameterizations are necessary. Significant progress has been made over the last two decades with advancements in computational capabilities, such as incorporating heterogeneous stress and friction conditions on a planar fault (e.g., Ripperger et al., 2007, 2008; Baumann & Dalguer, 2014; Andrews & Ma, 2016; Gallovič & Valentová, 2023) and fault roughness (e.g., Withers, Olsen, Day, & Shi, 2018; Withers, Olsen, Shi, & Day, 2018; Taufiqurrahman et al., 2022). However, we suspect that neither the planar-heterogeneity nor the fault roughness parameterizations are sufficient to explain the loss of radiation polarity at 0.4 Hz, as observed in the 2023 Mw 7.8 Kahramanmaraş earthquake (Section 5.1.1, Section 5.1.2). Additional mechanisms, such as dynamically-triggered off-fault structures (Section 5.1.3), low-velocity fault zone (Section 5.1.4), patchy anomalies in the near-fault velocity structure (Section 5.1.5), and elastic collision of discrete fault zone structures (Section 5.1.6), might help explain the observations.

6 Conclusion

In this study, we investigated the near-field strong-motion acceleration records of the 2023 Mw 7.8 Kahramanmaraş earthquake and explored its high-frequency radiation mechanisms. We observed a loss of horizontal polarity for radiation above ~ 0.4 Hz, suggesting that additional mechanisms near the fault, operating at smaller wavelengths, are needed to generate radiation in addition to the double-couple radiation produced by the main rupture front. At ~ 0.4 Hz, we also observed a loss of signal coherence between horizontal components, indicating that these small-scale mechanisms contribute to the transition from coherent low-frequency radiation to stochastic high-frequency radiation. The ~ 0.4 Hz transition boundary between low- and high-frequency radiation is lower than the commonly accepted rule-of-thumb value of 1 Hz.

Spectrograms from the near-fault stations show that high- and low-frequency radiation arrive simultaneously. Given their proximity to the fault, the recorded high-frequency radiation likely originated from the rupture front, rather than from scattering sources away from the fault or significantly behind the rupture front. At regional and teleseismic distances, scattering and attenuation may strongly alter high-frequency waveforms. Nevertheless, imprints of the source radiation may still be preserved, which could potentially be extracted using a specific method.

We summarize six types of high-frequency radiation mechanisms at or near the source and discuss their applicability in explaining the observed high-frequency characteristics of this earthquake. We suspect that the commonly used mechanism, which incorporates heterogeneous rupture parameters on a planar fault, may not be sufficient to explain the observed loss of horizontal polarity. Other mechanisms are conceptually possible; however, the quantitative tools needed to thoroughly test these potential mechanisms against observations are currently lacking. To first order, the ~ 0.4 Hz transition frequency corresponds to a complexity wavelength of 5-10 km, assuming a characteristic wave speed of 2-4 km/s. This suggests that the high-frequency radiation mechanism may extend up to a wavelength of 5-10 km. Our results highlight the need for improved earthquake source parameterization to assess high-frequency ground motion hazards and may provide valuable constraints for future theoretical studies on high-frequency radiation mechanisms.

Open Research Section

The strong motion data used in this research were obtained from the Disaster and Emergency Management Authority (AFAD), Türkiye, at `https://tadas.afad.gov.tr/event-detail/17966` (last accessed May 2024).

Acknowledgments

This research was inspired by a seminar delivered by Dr. Robert W. Graves at the University of Southern California in March 2024, as well as the subsequent discussion led by Dr. Yehuda Ben-Zion. We would like to thank Dr. Robert W. Graves, Dr. Yehuda Ben-Zion, Dr. Xiaofeng Meng, Siyuan Zhang, Dr. Sylvain Barbot, Dr. Sezim Güvercin, Binhao Wang, and Rachel Preca Trapani for their insightful discussions throughout the project. Our sincere thanks also go to Dr. Yuehua Zeng, Dr. Chen Ji, and Dr. Paul Martin Mai for their valuable feedback on our preliminary results. B. W. acknowledges support from the National Science Foundation award EAR-1848192, under Dr. Sylvain Barbot's research group at the University of Southern California, as well as from the John W. Miles Postdoctoral Fellowship at the University of California, San Diego. A.-A. G. acknowledges support from Horizon Europe (ChEESE-2P, grant number 101093038, DT-GEO, grant number 101058129, and Geo-INQUIRE, grant number 101058518), the National Aeronautics and Space Administration (80NSSC20K0495), the National Science Foundation (grant numbers EAR-2225286, EAR-2121568, OAC-2139536, OAC-2311208) and the Statewide California Earthquake Center (SCEC award 24103).

References

Abdelmeguid, M., Zhao, C., Yalcinkaya, E., Gazetas, G., Elbanna, A., & Rosakis, A. (2023, Dec 05). Dynamics of episodic supershear in the 2023 m7.8 kahramanmaraş/pazarcik earthquake, revealed by near-field records and computational modeling. *Communications Earth & Environment*, *4*(1), 456. Retrieved from `https://doi.org/10.1038/s43247-023-01131-7` doi: 10.1038/s43247-023-01131-7

Achenbach, J. D., & Harris, J. G. (1978). Ray method for elastodynamic radiation from a slip zone of arbitrary shape. *Journal of Geophysical Research: Solid Earth*, *83*(B5), 2283-2291. Retrieved from `https://agupubs.onlinelibrary.wiley.com/doi/abs/10.1029/JB083iB05p02283` doi: https://doi.org/10.1029/JB083iB05p02283

Adda-Bedia, M., & Madariaga, R. (2008, 10). Seismic radiation from a kink on an antiplane fault. *Bulletin of the Seismological Society of America*, *98*(5), 2291-2302. Retrieved from `https://doi.org/10.1785/0120080003` doi: 10.1785/0120080003

Aki, K. (1967). Scaling law of seismic spectrum. *Journal of Geophysical Research (1896-1977)*, *72*(4), 1217-1231. Retrieved from `https://agupubs.onlinelibrary.wiley.com/doi/abs/10.1029/JZ072i004p01217` doi: https://doi.org/10.1029/JZ072i004p01217

Aki, K. (2003). A perspective on the history of strong motion seismology. *Physics of the Earth and Planetary Interiors*, *137*(1), 5-11. Retrieved from `https://www.sciencedirect.com/science/article/pii/S0031920103000049` (The quantitative prediction of strong-motion and the physics of earthquake sources) doi: https://doi.org/10.1016/S0031-9201(03)00004-9

Akinci, A., Dindar, A. A., Bal, I. E., Ertuncay, D., Smyrou, E., & Cheloni, D. (2025, Jan 01). Characteristics of strong ground motions and structural damage patterns from the february 6th, 2023 kahramanmaraş earthquakes, türkiye. *Natural Hazards*, *121*(2), 1209-1239. Retrieved from https://doi.org/10.1007/s11069-024-06856-y doi: 10.1007/s11069-024-06856-y

Andrews, D. J. (1981). A stochastic fault model: 2. time-dependent case. *Journal of Geophysical Research: Solid Earth*, *86*(B11), 10821-10834. Retrieved from https://agupubs.onlinelibrary.wiley.com/doi/abs/10.1029/JB086iB11p10821 doi: https://doi.org/10.1029/JB086iB11p10821

Andrews, D. J., & Ma, S. (2016, 03). Validating a dynamic earthquake model to produce realistic ground motion. *Bulletin of the Seismological Society of America*, *106*(2), 665-672. Retrieved from https://doi.org/10.1785/0120150251 doi: 10.1785/0120150251

Antoine, S. L., Klinger, Y., Wang, K., & Bürgmann, R. (2024). Coseismic shallow slip deficit accounted for by diffuse off-fault deformation. *Geophysical Research Letters*, *51*(24), e2024GL110798. Retrieved from https://agupubs.onlinelibrary.wiley.com/doi/abs/10.1029/2024GL110798 (e2024GL110798 2024GL110798) doi: https://doi.org/10.1029/2024GL110798

Bao, H., Ampuero, J.-P., Meng, L., Fielding, E. J., Liang, C., Milliner, C. W. D., … Huang, H. (2019, Mar 01). Early and persistent supershear rupture of the 2018 magnitude 7.5 palu earthquake. *Nature Geoscience*, *12*(3), 200-205. Retrieved from https://doi.org/10.1038/s41561-018-0297-z doi: 10.1038/s41561-018-0297-z

Bao, H., Xu, L., Meng, L., Ampuero, J.-P., Gao, L., & Zhang, H. (2022, Nov 01). Global frequency of oceanic and continental supershear earthquakes. *Nature Geoscience*, *15*(11), 942-949. Retrieved from https://doi.org/10.1038/s41561-022-01055-5 doi: 10.1038/s41561-022-01055-5

Barbot, S., Luo, H., Wang, T., Hamiel, Y., Piatibratova, O., Javed, M. T., … Gurbuz, G. (2023, Apr.). Slip distribution of the february 6, 2023 mw 7.8 and mw 7.6, kahramanmaraş, turkey earthquake sequence in the east anatolian fault zone. *Seismica*, *2*(3). Retrieved from https://seismica.library.mcgill.ca/article/view/502 doi: 10.26443/seismica.v2i3.502

Baumann, C., & Dalguer, L. A. (2014, 03). Evaluating the compatibility of dynamic rupture-based synthetic ground motion with empirical ground-motion prediction equation. *Bulletin of the Seismological Society of America*, *104*(2), 634-652. Retrieved from https://doi.org/10.1785/0120130077 doi: 10.1785/0120130077

Bayless, J. R. (2018). *Inter-period correlations of fourier amplitude spectra of ground-motions : modeling, calibration of earthquake simulations, and significance in seismic risk.* Davis, Calif: University of California, Davis.

Ben-Zion, Y. (1998). Properties of seismic fault zone waves and their utility for imaging low-velocity structures. *Journal of Geophysical Research: Solid Earth*, *103*(B6), 12567-12585. Retrieved from https://agupubs.onlinelibrary.wiley.com/doi/abs/10.1029/98JB00768 doi: https://doi.org/10.1029/98JB00768

Ben-Zion, Y., & Ampuero, J.-P. (2009, 09). Seismic radiation from regions sustaining material damage. *Geophysical Journal International*, *178*(3), 1351-1356. Retrieved from https://doi.org/10.1111/j.1365-246X.2009.04285.x doi: 10.1111/j.1365-246X.2009.04285.x

Ben-Zion, Y., Peng, Z., Okaya, D., Seeber, L., Armbruster, J. G., Ozer, N., … Aktar, M. (2003, 03). A shallow fault-zone structure illuminated by trapped waves in the karadere–duzce branch of the north anatolian fault, western turkey. *Geophysical Journal International*, *152*(3), 699-717. Retrieved from https://doi.org/10.1046/j.1365-246X.2003.01870.x doi: 10.1046/j.1365-246X.2003.01870.x

Ben-Zion, Y., Zhang, S., & Meng, X. (2024). Isotropic high-frequency radiation in near-fault seismic data. *Geophysical Research Letters*, *51*(17), e2024GL110303.

Retrieved from https://agupubs.onlinelibrary.wiley.com/doi/abs/10.1029/2024GL110303 (e2024GL110303 2024GL110303) doi: https://doi.org/10.1029/2024GL110303

Bernard, P., & Madariaga, R. (1984, 04). A new asymptotic method for the modeling of near-field accelerograms. *Bulletin of the Seismological Society of America*, *74*(2), 539-557. Retrieved from https://doi.org/10.1785/BSSA0740020539 doi: 10.1785/BSSA0740020539

Boatwright, J. (1982, 08). A dynamic model for far-field acceleration. *Bulletin of the Seismological Society of America*, *72*(4), 1049-1068. Retrieved from https://doi.org/10.1785/BSSA0720041049 doi: 10.1785/BSSA0720041049

Boatwright, J. (1988, 04). The seismic radiation from composite models of faulting. *Bulletin of the Seismological Society of America*, *78*(2), 489-508. Retrieved from https://doi.org/10.1785/BSSA0780020489 doi: 10.1785/BSSA0780020489

Boore, D. M. (1983, 12). Stochastic simulation of high-frequency ground motions based on seismological models of the radiated spectra. *Bulletin of the Seismological Society of America*, *73*(6A), 1865-1894. Retrieved from https://doi.org/10.1785/BSSA07306A1865 doi: 10.1785/BSSA07306A1865

Boore, D. M. (2003, Mar 01). Simulation of ground motion using the stochastic method. *pure and applied geophysics*, *160*(3), 635-676. Retrieved from https://doi.org/10.1007/PL00012553 doi: 10.1007/PL00012553

Brune, J. N. (1970). Tectonic stress and the spectra of seismic shear waves from earthquakes. *Journal of Geophysical Research (1896-1977)*, *75*(26), 4997-5009. Retrieved from https://agupubs.onlinelibrary.wiley.com/doi/abs/10.1029/JB075i026p04997 doi: https://doi.org/10.1029/JB075i026p04997

Castro, R. R., & Ben-Zion, Y. (2013, 04). Potential signatures of damage-related radiation from aftershocks of the 4 april 2010 (mw 7.2) el mayor–cucapah earthquake, baja california, méxico. *Bulletin of the Seismological Society of America*, *103*(2A), 1130-1140. Retrieved from https://doi.org/10.1785/0120120163 doi: 10.1785/0120120163

Castro, R. R., Franceschina, G., Pacor, F., Bindi, D., & Luzi, L. (2006, 04). Analysis of the frequency dependence of the s-wave radiation pattern from local earthquakes in central italy. *Bulletin of the Seismological Society of America*, *96*(2), 415-426. Retrieved from https://doi.org/10.1785/0120050066 doi: 10.1785/0120050066

Čejka, F., Zahradník, J., Turhan, F., Sokos, E., & Gallovič, F. (2023, Nov 11). Long-period directivity pulses of strong ground motion during the 2023 mw7.8 kahramanmaraş earthquake. *Communications Earth & Environment*, *4*(1), 413. Retrieved from https://doi.org/10.1038/s43247-023-01076-x doi: 10.1038/s43247-023-01076-x

Chen, W., Rao, G., Kang, D., Wan, Z., & Wang, D. (2023, Apr 01). Early report of the source characteristics, ground motions, and casualty estimates of the 2023 mw 7.8 and 7.5 turkey earthquakes. *Journal of Earth Science*, *34*(2), 297-303. Retrieved from https://doi.org/10.1007/s12583-023-1316-6 doi: 10.1007/s12583-023-1316-6

Chen, W., Wang, D., Si, H., & Zhang, C. (2022, 03). Rapid estimation of seismic intensities using a new algorithm that incorporates array technologies and ground-motion prediction equations (gmpes). *Bulletin of the Seismological Society of America*, *112*(3), 1647-1661. Retrieved from https://doi.org/10.1785/0120210207 doi: 10.1785/0120210207

Chester, F. M., & Chester, J. S. (1998). Ultracataclasite structure and friction processes of the punchbowl fault, san andreas system, california. *Tectonophysics*, *295*(1), 199-221. Retrieved from https://www.sciencedirect.com/science/article/pii/S0040195198001218 doi: https://doi.org/10.1016/S0040-1951(98)00121-8

Cochran, E. S., Li, Y.-G., Shearer, P. M., Barbot, S., Fialko, Y., & Vidale, J. E. (2009, 04). Seismic and geodetic evidence for extensive, long-lived fault damage zones. *Geology*, *37*(4), 315-318. Retrieved from https://doi.org/10.1130/G25306A.1 doi: 10.1130/G25306A.1

Ding, X., Xu, S., Xie, Y., van den Ende, M., Premus, J., & Ampuero, J.-P. (2023, November). The sharp turn: Backward rupture branching during the 2023 Mw 7.8 Kahramanmaraş (Türkiye) earthquake. *Seismica*, *2*(3). Retrieved from https://hal.science/hal-04391440 doi: 10.26443/seismica.v2i3.1083

Dunham, E. M., & Archuleta, R. J. (2004, 12). Evidence for a supershear transient during the 2002 denali fault earthquake. *Bulletin of the Seismological Society of America*, *94*(6B), S256-S268. Retrieved from https://doi.org/10.1785/0120040616 doi: 10.1785/0120040616

Dunham, E. M., & Archuleta, R. J. (2005). Near-source ground motion from steady state dynamic rupture pulses. *Geophysical Research Letters*, *32*(3). Retrieved from https://agupubs.onlinelibrary.wiley.com/doi/abs/10.1029/2004GL021793 doi: https://doi.org/10.1029/2004GL021793

Dunham, E. M., Belanger, D., Cong, L., & Kozdon, J. E. (2011, 10). Earthquake ruptures with strongly rate-weakening friction and off-fault plasticity, part 2: Nonplanar faults. *Bulletin of the Seismological Society of America*, *101*(5), 2308-2322. Retrieved from https://doi.org/10.1785/0120100076 doi: 10.1785/0120100076

Erdik, M., Tümsa, M. B. D., Pınar, A., Altunel, E., & Zülfikar, A. C. (2023). *A preliminary report on the february 6, 2023 earthquakes in türkiye.* Retrieved from http://doi.org/10.32858/temblor.297 doi: 10.32858/temblor.297

Fan, W., & Shearer, P. M. (2015). Detailed rupture imaging of the 25 april 2015 nepal earthquake using teleseismic p waves. *Geophysical Research Letters*, *42*(14), 5744-5752. Retrieved from https://agupubs.onlinelibrary.wiley.com/doi/abs/10.1002/2015GL064587 doi: https://doi.org/10.1002/2015GL064587

Faulkner, D., Lewis, A., & Rutter, E. (2003). On the internal structure and mechanics of large strike-slip fault zones: field observations of the carboneras fault in southeastern spain. *Tectonophysics*, *367*(3), 235-251. Retrieved from https://www.sciencedirect.com/science/article/pii/S0040195103001343 doi: https://doi.org/10.1016/S0040-1951(03)00134-3

Feng, T., & Meng, L. (2018). A high-frequency distance metric in ground-motion prediction equations based on seismic array backprojections. *Geophysical Research Letters*, *45*(21), 11,612-11,621. Retrieved from https://agupubs.onlinelibrary.wiley.com/doi/abs/10.1029/2018GL078930 doi: https://doi.org/10.1029/2018GL078930

Fialko, Y., Sandwell, D., Simons, M., & Rosen, P. (2005, May 01). Three-dimensional deformation caused by the bam, iran, earthquake and the origin of shallow slip deficit. *Nature*, *435*(7040), 295-299. Retrieved from https://doi.org/10.1038/nature03425 doi: 10.1038/nature03425

Frankel, A. (1991). High-frequency spectral falloff of earthquakes, fractal dimension of complex rupture, b value, and the scaling of strength on faults. *Journal of Geophysical Research: Solid Earth*, *96*(B4), 6291-6302. Retrieved from https://agupubs.onlinelibrary.wiley.com/doi/abs/10.1029/91JB00237 doi: https://doi.org/10.1029/91JB00237

Frankel, A. (1995, 08). Simulating strong motions of large earthquakes using recordings of small earthquakes: the loma prieta mainshock as a test case. *Bulletin of the Seismological Society of America*, *85*(4), 1144-1160. Retrieved from https://doi.org/10.1785/BSSA0850041144 doi: 10.1785/BSSA0850041144

Frankel, A. (2009, 04). A constant stress-drop model for producing broadband synthetic seismograms: Comparison with the next generation attenuation relations. *Bulletin of the Seismological Society of America*, *99*(2A),

664-680. Retrieved from https://doi.org/10.1785/0120080079 doi: 10.1785/0120080079
Gabriel, A., Ulrich, T., Marchandon, M., Biemiller, J., & Rekoske, J. (2023, 12). 3d dynamic rupture modeling of the 6 february 2023, kahramanmaraş, turkey mw 7.8 and 7.7 earthquake doublet using early observations. *The Seismic Record*, *3*(4), 342-356. Retrieved from https://doi.org/10.1785/0320230028 doi: 10.1785/0320230028
Gallovič, F., & Valentová, Ľ. (2023, Jun 01). Broadband strong ground motion modeling using planar dynamic rupture with fractal parameters. *Journal of Geophysical Research: Solid Earth*, *128*(6), e2023JB026506. Retrieved from https://doi.org/10.1029/2023JB026506 doi: 10.1029/2023JB026506
Gallovič, F., & Brokešová, J. (2007). Hybrid k-squared source model for strong ground motion simulations: Introduction. *Physics of the Earth and Planetary Interiors*, *160*(1), 34-50. Retrieved from https://www.sciencedirect.com/science/article/pii/S0031920106002822 doi: https://doi.org/10.1016/j.pepi.2006.09.002
Graves, R. W., & Pitarka, A. (2010, 10). Broadband ground-motion simulation using a hybrid approach. *Bulletin of the Seismological Society of America*, *100*(5A), 2095-2123. Retrieved from https://doi.org/10.1785/0120100057 doi: 10.1785/0120100057
Graves, R. W., & Pitarka, A. (2016, 08). Kinematic ground-motion simulations on rough faults including effects of 3d stochastic velocity perturbations. *Bulletin of the Seismological Society of America*, *106*(5), 2136-2153. Retrieved from https://doi.org/10.1785/0120160088 doi: 10.1785/0120160088
Güvercin, S. E. (2024, 01). 2023 earthquake doublet in türkiye reveals the complexities of the east anatolian fault zone: Insights from aftershock patterns and moment tensor solutions. *Seismological Research Letters*, *95*(2A), 664-679. Retrieved from https://doi.org/10.1785/0220230317 doi: 10.1785/0220230317
Güvercin, S. E., Karabulut, H., Konca, A. Ö., Doğan, U., & Ergintav, S. (2022, Jul 01). Active seismotectonics of the east anatolian fault. *Geophysical Journal International*, *230*(1), 50-69. Retrieved from https://doi.org/10.1093/gji/ggac045 doi: 10.1093/gji/ggac045
Hanks, T. C. (1979). b values and $\omega - \gamma$ seismic source models: Implications for tectonic stress variations along active crustal fault zones and the estimation of high-frequency strong ground motion. *Journal of Geophysical Research: Solid Earth*, *84*(B5), 2235-2242. Retrieved from https://agupubs.onlinelibrary.wiley.com/doi/abs/10.1029/JB084iB05p02235 doi: https://doi.org/10.1029/JB084iB05p02235
Hanks, T. C., & McGuire, R. K. (1981, 12). The character of high-frequency strong ground motion. *Bulletin of the Seismological Society of America*, *71*(6), 2071-2095. Retrieved from https://doi.org/10.1785/BSSA0710062071 doi: 10.1785/BSSA0710062071
Harris, R. A., Barall, M., Aagaard, B., Ma, S., Roten, D., Olsen, K., … Dalguer, L. (2018, 04). A suite of exercises for verifying dynamic earthquake rupture codes. *Seismological Research Letters*, *89*(3), 1146-1162. Retrieved from https://doi.org/10.1785/0220170222 doi: 10.1785/0220170222
Harris, R. A., & Day, S. M. (1997, 10). Effects of a low-velocity zone on a dynamic rupture. *Bulletin of the Seismological Society of America*, *87*(5), 1267-1280. Retrieved from https://doi.org/10.1785/BSSA0870051267 doi: 10.1785/BSSA0870051267
Hartzell, S., Harmsen, S., Frankel, A., & Larsen, S. (1999, 12). Calculation of broadband time histories of ground motion: Comparison of methods and validation using strong-ground motion from the 1994 northridge earthquake. *Bulletin of the Seismological Society of America*, *89*(6), 1484-1504. Retrieved from

https://doi.org/10.1785/BSSA0890061484 doi: 10.1785/BSSA0890061484

Haskell, N. A. (1964, 12). Total energy and energy spectral density of elastic wave radiation from propagating faults. *Bulletin of the Seismological Society of America*, *54*(6A), 1811-1841. Retrieved from https://doi.org/10.1785/BSSA05406A1811 doi: 10.1785/BSSA05406A1811

He, Z., Zhang, Z., Wang, Z., & Wang, W. (2024). Slip-weakening distance and energy partitioning estimated from near-fault recordings during the 2023 mw 7.8 türkiye-syria earthquake. *Tectonophysics*, *885*, 230424. Retrieved from https://www.sciencedirect.com/science/article/pii/S0040195124002269 doi: https://doi.org/10.1016/j.tecto.2024.230424

Housner, G. W. (1947, 01). Characteristics of strong-motion earthquakes*. *Bulletin of the Seismological Society of America*, *37*(1), 19-31. Retrieved from https://doi.org/10.1785/BSSA0370010019 doi: 10.1785/BSSA0370010019

Housner, G. W., & Trifunac, M. D. (1967, 12). Analysis of accelerograms—parkfield earthquake. *Bulletin of the Seismological Society of America*, *57*(6), 1193-1220. Retrieved from https://doi.org/10.1785/BSSA0570061193 doi: 10.1785/BSSA0570061193

Hu, F., Oglesby, D. D., & Chen, X. (2019). The sustainability of free-surface-induced supershear rupture on strike-slip faults. *Geophysical Research Letters*, *46*(16), 9537-9543. Retrieved from https://agupubs.onlinelibrary.wiley.com/doi/abs/10.1029/2019GL084318 doi: https://doi.org/10.1029/2019GL084318

Hu, F., Wen, J., & Chen, X. (2018). High frequency near-field ground motion excited by strike-slip step overs. *Journal of Geophysical Research: Solid Earth*, *123*(3), 2303-2317. Retrieved from https://agupubs.onlinelibrary.wiley.com/doi/abs/10.1002/2017JB015027 doi: https://doi.org/10.1002/2017JB015027

Huang, Y., Ampuero, J.-P., & Helmberger, D. V. (2014). Earthquake ruptures modulated by waves in damaged fault zones. *Journal of Geophysical Research: Solid Earth*, *119*(4), 3133-3154. Retrieved from https://agupubs.onlinelibrary.wiley.com/doi/abs/10.1002/2013JB010724 doi: https://doi.org/10.1002/2013JB010724

Imperatori, W., & Mai, P. M. (2012, 12). Broad-band near-field ground motion simulations in 3-dimensional scattering media. *Geophysical Journal International*, *192*(2), 725-744. Retrieved from https://doi.org/10.1093/gji/ggs041 doi: 10.1093/gji/ggs041

Irikura, K., & Miyake, H. (2011, Jan 01). Recipe for predicting strong ground motion from crustal earthquake scenarios. *Pure and Applied Geophysics*, *168*(1), 85-104. Retrieved from https://doi.org/10.1007/s00024-010-0150-9 doi: 10.1007/s00024-010-0150-9

Ishii, M., Shearer, P. M., Houston, H., & Vidale, J. E. (2005, Jun 01). Extent, duration and speed of the 2004 sumatra–andaman earthquake imaged by the hi-net array. *Nature*, *435*(7044), 933-936. Retrieved from https://doi.org/10.1038/nature03675 doi: 10.1038/nature03675

Jia, Z., Jin, Z., Marchandon, M., Ulrich, T., Gabriel, A.-A., Fan, W., … Fialko, Y. (2023). The complex dynamics of the 2023 kahramanmaraş, turkey, ¡i¿m¡/i¿¡sub¿w¡/sub¿ 7.8-7.7 earthquake doublet. *Science*, *381*(6661), 985-990. Retrieved from https://www.science.org/doi/abs/10.1126/science.adi0685 doi: 10.1126/science.adi0685

Kamae, K., Irikura, K., & Pitarka, A. (1998, 04). A technique for simulating strong ground motion using hybrid green's function. *Bulletin of the Seismological Society of America*, *88*(2), 357-367. Retrieved from https://doi.org/10.1785/BSSA0880020357 doi: 10.1785/BSSA0880020357

Kiser, E., & Ishii, M. (2011). The 2010 mw 8.8 chile earthquake: Triggering on multiple segments and frequency-dependent rupture behavior. *Geophysical*

Research Letters, *38*(7). Retrieved from https://agupubs.onlinelibrary.wiley.com/doi/abs/10.1029/2011GL047140 doi: https://doi.org/10.1029/2011GL047140

Kobayashi, M., Takemura, S., & Yoshimoto, K. (2015, 07). Frequency and distance changes in the apparent p-wave radiation pattern: effects of seismic wave scattering in the crust inferred from dense seismic observations and numerical simulations. *Geophysical Journal International*, *202*(3), 1895-1907. Retrieved from https://doi.org/10.1093/gji/ggv263 doi: 10.1093/gji/ggv263

Kobayashi, T., Munekane, H., Kuwahara, M., & Furui, H. (2024, Feb 01). Insights on the 2023 kahramanmaraş earthquake, turkey, from insar: fault locations, rupture styles and induced deformation. *Geophysical Journal International*, *236*(2), 1068-1088. Retrieved from https://doi.org/10.1093/gji/ggad464 doi: 10.1093/gji/ggad464

Koper, K. D., Hutko, A. R., Lay, T., Ammon, C. J., & Kanamori, H. (2011, Jul 01). Frequency-dependent rupture process of the 2011 mw 9.0 tohoku earthquake: Comparison of short-period p wave backprojection images and broadband seismic rupture models. *Earth, Planets and Space*, *63*(7), 599-602. Retrieved from https://doi.org/10.5047/eps.2011.05.026 doi: 10.5047/eps.2011.05.026

Kotha, S. R., Cotton, F., & Bindi, D. (2019, Jan 30). Empirical models of shear-wave radiation pattern derived from large datasets of ground-shaking observations. *Scientific Reports*, *9*(1), 981. Retrieved from https://doi.org/10.1038/s41598-018-37524-4 doi: 10.1038/s41598-018-37524-4

Krüger, F., & Ohrnberger, M. (2005, Jun 01). Tracking the rupture of the mw = 9.3 sumatra earthquake over 1,150 km at teleseismic distance. *Nature*, *435*(7044), 937-939. Retrieved from https://doi.org/10.1038/nature03696 doi: 10.1038/nature03696

Lay, T., Kanamori, H., Ammon, C. J., Koper, K. D., Hutko, A. R., Ye, L., … Rushing, T. M. (2012). Depth-varying rupture properties of subduction zone megathrust faults. *Journal of Geophysical Research: Solid Earth*, *117*(B4). Retrieved from https://agupubs.onlinelibrary.wiley.com/doi/abs/10.1029/2011JB009133 doi: https://doi.org/10.1029/2011JB009133

Li, B., & Ghosh, A. (2017). Imaging rupture process of the 2015 mw 8.3 illapel earthquake using the us seismic array. In C. Braitenberg & A. B. Rabinovich (Eds.), *The chile-2015 (illapel) earthquake and tsunami* (pp. 33–43). Cham: Springer International Publishing. Retrieved from https://doi.org/10.1007/978-3-319-57822-4_4 doi: 10.1007/978-3-319-57822-4_4

Li, B., Palgunadi, K. H., Wu, B., Suhendi, C., Zhou, Y., Ghosh, A., & Mai, P. M. (2025, Mar 23). Rupture dynamics and velocity structure effects on ground motion during the 2023 türkiye earthquake doublet. *Communications Earth & Environment*, *6*(1), 228. Retrieved from https://doi.org/10.1038/s43247-025-02205-4 doi: 10.1038/s43247-025-02205-4

Li, B., Wu, B., Bao, H., Oglesby, D. D., Ghosh, A., Gabriel, A.-A., … Chu, R. (2022). Rupture heterogeneity and directivity effects in back-projection analysis. *Journal of Geophysical Research: Solid Earth*, *127*(3), e2021JB022663. Retrieved from https://agupubs.onlinelibrary.wiley.com/doi/abs/10.1029/2021JB022663 (e2021JB022663 2021JB022663) doi: https://doi.org/10.1029/2021JB022663

Li, Y.-G., Aki, K., Adams, D., Hasemi, A., & Lee, W. H. K. (1994). Seismic guided waves trapped in the fault zone of the landers, california, earthquake of 1992. *Journal of Geophysical Research: Solid Earth*, *99*(B6), 11705-11722. Retrieved from https://agupubs.onlinelibrary.wiley.com/doi/abs/10.1029/94JB00464 doi: https://doi.org/10.1029/94JB00464

Li, Y.-G., Leary, P., Aki, K., & Malin, P. (1990). Seismic trapped modes in the oroville and san andreas fault zones. *Science*, *249*(4970), 763-766. Retrieved from https://www.science.org/doi/abs/10.1126/science.249.4970.763

doi: 10.1126/science.249.4970.763
Li, Y.-G., & Vidale, J. E. (1996, 04). Low-velocity fault-zone guided waves: Numerical investigations of trapping efficiency. *Bulletin of the Seismological Society of America*, *86*(2), 371-378. Retrieved from https://doi.org/10.1785/BSSA0860020371 doi: 10.1785/BSSA0860020371
Li, Y.-G., Vidale, J. E., & Cochran, E. S. (2004). Low-velocity damaged structure of the san andreas fault at parkfield from fault zone trapped waves. *Geophysical Research Letters*, *31*(12). Retrieved from https://agupubs.onlinelibrary.wiley.com/doi/abs/10.1029/2003GL019044 doi: https://doi.org/10.1029/2003GL019044
Lin, Y.-P., & Jordan, T. H. (2023). Elastic scattering dominates high-frequency seismic attenuation in southern california. *Earth and Planetary Science Letters*, *616*, 118227. Retrieved from https://www.sciencedirect.com/science/article/pii/S0012821X23002406 doi: https://doi.org/10.1016/j.epsl.2023.118227
Liu, C., Lay, T., Wang, R., Taymaz, T., Xie, Z., Xiong, X., … Erman, C. (2023, Sep 09). Complex multi-fault rupture and triggering during the 2023 earthquake doublet in southeastern türkiye. *Nature Communications*, *14*(1), 5564. Retrieved from https://doi.org/10.1038/s41467-023-41404-5 doi: 10.1038/s41467-023-41404-5
Liu, J., Huang, C., Zhang, G., Shan, X., Korzhenkov, A., & Taymaz, T. (2024, May 09). Immature characteristics of the east anatolian fault zone from sar, gnss and strong motion data of the 2023 türkiye–syria earthquake doublet. *Scientific Reports*, *14*(1), 10625. Retrieved from https://doi.org/10.1038/s41598-024-61326-6 doi: 10.1038/s41598-024-61326-6
Liu, J., Jónsson, S., Li, X., Yao, W., & Klinger, Y. (2025, Feb 03). Extensive off-fault damage around the 2023 kahramanmaraş earthquake surface ruptures. *Nature Communications*, *16*(1), 1286. Retrieved from https://doi.org/10.1038/s41467-025-56466-w doi: 10.1038/s41467-025-56466-w
Liu, P., Archuleta, R. J., & Hartzell, S. H. (2006, 12). Prediction of broadband ground-motion time histories: Hybrid low/high- frequency method with correlated random source parameters. *Bulletin of the Seismological Society of America*, *96*(6), 2118-2130. Retrieved from https://doi.org/10.1785/0120060036 doi: 10.1785/0120060036
Loth, C., & Baker, J. W. (2013). A spatial cross-correlation model of spectral accelerations at multiple periods. *Earthquake Engineering & Structural Dynamics*, *42*(3), 397-417. Retrieved from https://onlinelibrary.wiley.com/doi/abs/10.1002/eqe.2212 doi: https://doi.org/10.1002/eqe.2212
Lozos, J., Akçiz, S., & Ladage, H. (2025). Modeling the rupture dynamics of strong ground motion (¿ 1 g) in fault stepovers. *Tectonophysics*, *895*, 230580. Retrieved from https://www.sciencedirect.com/science/article/pii/S0040195124003822 doi: https://doi.org/10.1016/j.tecto.2024.230580
Ma, Z., Li, C., Jiang, Y., Chen, Y., Yin, X., Aoki, Y., … Wei, S. (2024). Space geodetic insights to the dramatic stress rotation induced by the february 2023 turkey-syria earthquake doublet. *Geophysical Research Letters*, *51*(6), e2023GL107788. Retrieved from https://agupubs.onlinelibrary.wiley.com/doi/abs/10.1029/2023GL107788 (e2023GL107788 2023GL107788) doi: https://doi.org/10.1029/2023GL107788
Madariaga, R. (1976, 06). Dynamics of an expanding circular fault. *Bulletin of the Seismological Society of America*, *66*(3), 639-666. Retrieved from https://doi.org/10.1785/BSSA0660030639 doi: 10.1785/BSSA0660030639
Madariaga, R. (1977, 12). High-frequency radiation from crack (stress drop) models of earthquake faulting. *Geophysical Journal International*, *51*(3), 625-651. Retrieved from https://doi.org/10.1111/j.1365-246X.1977.tb04211.x doi: 10.1111/j.1365-246X.1977.tb04211.x

Madariaga, R., Ruiz, S., Rivera, E., Leyton, F., & Baez, J. C. (2019, Mar 01). Near-field spectra of large earthquakes. *Pure and Applied Geophysics*, *176*(3), 983-1001. Retrieved from https://doi.org/10.1007/s00024-018-1983-x doi: 10.1007/s00024-018-1983-x

Mai, P. M., Aspiotis, T., Aquib, T. A., Cano, E. V., Castro-Cruz, D., Espindola-Carmona, A., ... Jónsson, S. (2023, 05). The destructive earthquake doublet of 6 february 2023 in south-central türkiye and northwestern syria: Initial observations and analyses. *The Seismic Record*, *3*(2), 105-115. Retrieved from https://doi.org/10.1785/0320230007 doi: 10.1785/0320230007

Mai, P. M., Galis, M., Thingbaijam, K. K. S., Vyas, J. C., & Dunham, E. M. (2018). Accounting for fault roughness in pseudo-dynamic ground-motion simulations. In L. A. Dalguer, Y. Fukushima, K. Irikura, & C. Wu (Eds.), *Best practices in physics-based fault rupture models for seismic hazard assessment of nuclear installations* (pp. 95–126). Cham: Springer International Publishing. Retrieved from https://doi.org/10.1007/978-3-319-72709-7_7 doi: 10.1007/978-3-319-72709-7_7

Mai, P. M., Imperatori, W., & Olsen, K. B. (2010, 10). Hybrid broadband ground-motion simulations: Combining long-period deterministic synthetics with high-frequency multiple s-to-s backscattering. *Bulletin of the Seismological Society of America*, *100*(5A), 2124-2142. Retrieved from https://doi.org/10.1785/0120080194 doi: 10.1785/0120080194

McGuire, R. K., & Hanks, T. C. (1980, 10). Rms accelerations and spectral amplitudes of strong ground motion during the san fernando, california earthquake. *Bulletin of the Seismological Society of America*, *70*(5), 1907-1919. Retrieved from https://doi.org/10.1785/BSSA0700051907 doi: 10.1785/BSSA0700051907

Melgar, D., Taymaz, T., Ganas, A., Crowell, B., Öcalan, T., Kahraman, M., ... Altuntaş, C. (2023, Mar.). Sub- and super-shear ruptures during the 2023 mw 7.8 and mw 7.6 earthquake doublet in se türkiye. *Seismica*, *2*(3). Retrieved from https://seismica.library.mcgill.ca/article/view/387 doi: 10.26443/seismica.v2i3.387

Mello, M., Bhat, H. S., & Rosakis, A. J. (2016). Spatiotemporal properties of sub-rayleigh and supershear rupture velocity fields: Theory and experiments. *Journal of the Mechanics and Physics of Solids*, *93*, 153-181. Retrieved from https://www.sciencedirect.com/science/article/pii/S0022509616301363 (Special Issue in honor of Michael Ortiz) doi: https://doi.org/10.1016/j.jmps.2016.02.031

Meng, J., Kusky, T., Mooney, W. D., Bozkurt, E., Bodur, M. N., & Wang, L. (2024). Surface deformations of the 6 february 2023 earthquake sequence, eastern türkiye. *Science*, *383*(6680), 298-305. Retrieved from https://www.science.org/doi/abs/10.1126/science.adj3770 doi: 10.1126/science.adj3770

Meng, L., Ampuero, J.-P., Stock, J., Duputel, Z., Luo, Y., & Tsai, V. C. (2012). Earthquake in a maze: Compressional rupture branching during the 2012 ¡i¿m¡/i¿¡sub¿w¡/sub¿ 8.6 sumatra earthquake. *Science*, *337*(6095), 724-726. Retrieved from https://www.science.org/doi/abs/10.1126/science.1224030 doi: 10.1126/science.1224030

Meng, L., Zhang, A., & Yagi, Y. (2016). Improving back projection imaging with a novel physics-based aftershock calibration approach: A case study of the 2015 gorkha earthquake. *Geophysical Research Letters*, *43*(2), 628-636. Retrieved from https://agupubs.onlinelibrary.wiley.com/doi/abs/10.1002/2015GL067034 doi: https://doi.org/10.1002/2015GL067034

Motazedian, D., & Atkinson, G. M. (2005, 06). Stochastic finite-fault modeling based on a dynamic corner frequency. *Bulletin of the Seismological Society of America*, *95*(3), 995-1010. Retrieved from https://doi.org/10.1785/

0120030207 doi: 10.1785/0120030207

Nagasaka, Y., & Nozu, A. (2024, 08). Kinematic source properties of the 2023 mw 7.7 türkiye earthquake inferred from near-fault strong ground motions. *Seismological Research Letters*, *96*(1), 19-34. Retrieved from https://doi.org/10.1785/0220240156 doi: 10.1785/0220240156

Okubo, K., Bhat, H. S., Rougier, E., Marty, S., Schubnel, A., Lei, Z., ... Klinger, Y. (2019). Dynamics, radiation, and overall energy budget of earthquake rupture with coseismic off-fault damage. *Journal of Geophysical Research: Solid Earth*, *124*(11), 11771-11801. Retrieved from https://agupubs.onlinelibrary.wiley.com/doi/abs/10.1029/2019JB017304 doi: https://doi.org/10.1029/2019JB017304

Palo, M., & Zollo, A. (2024, Aug 14). Small-scale segmented fault rupture along the east anatolian fault during the 2023 kahramanmaraş earthquake. *Communications Earth & Environment*, *5*(1), 431. Retrieved from https://doi.org/10.1038/s43247-024-01597-z doi: 10.1038/s43247-024-01597-z

Papageorgiou, A. S., & Aki, K. (1983a, 06). A specific barrier model for the quantitative description of inhomogeneous faulting and the prediction of strong ground motion. i. description of the model. *Bulletin of the Seismological Society of America*, *73*(3), 693-722. Retrieved from https://doi.org/10.1785/BSSA0730030693 doi: 10.1785/BSSA0730030693

Papageorgiou, A. S., & Aki, K. (1983b, 08). A specific barrier model for the quantitative description of inhomogeneous faulting and the prediction of strong ground motion. part ii. applications of the model. *Bulletin of the Seismological Society of America*, *73*(4), 953-978. Retrieved from https://doi.org/10.1785/BSSA0730040953 doi: 10.1785/BSSA0730040953

Petersen, G. M., Büyükakpinar, P., Vera Sanhueza, F. O., Metz, M., Cesca, S., Akbayram, K., ... Dahm, T. (2023, 05). The 2023 southeast türkiye seismic sequence: Rupture of a complex fault network. *The Seismic Record*, *3*(2), 134-143. Retrieved from https://doi.org/10.1785/0320230008 doi: 10.1785/0320230008

Provost, F., Karabacak, V., Malet, J.-P., Van der Woerd, J., Meghraoui, M., Masson, F., ... Pointal, E. (2024, Mar 21). High-resolution co-seismic fault offsets of the 2023 türkiye earthquake ruptures using satellite imagery. *Scientific Reports*, *14*(1), 6834. Retrieved from https://doi.org/10.1038/s41598-024-55009-5 doi: 10.1038/s41598-024-55009-5

Pulido, N., & Dalguer, L. A. (2009, 08). Estimation of the high-frequency radiation of the 2000 tottori (japan) earthquake based on a dynamic model of fault rupture: Application to the strong ground motion simulation. *Bulletin of the Seismological Society of America*, *99*(4), 2305-2322. Retrieved from https://doi.org/10.1785/0120080165 doi: 10.1785/0120080165

Reitman, N. G., Briggs, R. W., Barnhart, W. D., Hatem, A. E., Thompson Jobe, J. A., DuRoss, C. B., ... Akçiz, S. (2023, 11). Rapid surface rupture mapping from satellite data: The 2023 kahramanmaraş, turkey (türkiye), earthquake sequence. *The Seismic Record*, *3*(4), 289-298. Retrieved from https://doi.org/10.1785/0320230029 doi: 10.1785/0320230029

Reitman, N. G., Briggs, R. W., Barnhart, W. D., Thompson Jobe, J. A., DuRoss, C. B., Hatem, A. E., ... Collett, C. (2023, February). *Fault rupture mapping of the 6 february 2023 kahramanmaraş, türkiye, earthquake sequence from satellite data.* https://doi.org/10.5066/P985I7U2. U.S. Geological Survey. doi: 10.5066/P985I7U2

Ren, C., Wang, Z., Taymaz, T., Hu, N., Luo, H., Zhao, Z., ... Ding, H. (2024). Supershear triggering and cascading fault ruptures of the 2023 kahramanmaraş, türkiye, earthquake doublet. *Science*, *383*(6680), 305-311. Retrieved from https://www.science.org/doi/abs/10.1126/science.adi1519 doi: 10.1126/science.adi1519

Ripperger, J., Ampuero, J.-P., Mai, P. M., & Giardini, D. (2007). Earthquake source characteristics from dynamic rupture with constrained stochastic fault stress. *Journal of Geophysical Research: Solid Earth*, *112*(B4). Retrieved from `https://agupubs.onlinelibrary.wiley.com/doi/abs/10.1029/2006JB004515` doi: https://doi.org/10.1029/2006JB004515

Ripperger, J., Mai, P. M., & Ampuero, J.-P. (2008, 06). Variability of near-field ground motion from dynamic earthquake rupture simulations. *Bulletin of the Seismological Society of America*, *98*(3), 1207-1228. Retrieved from `https://doi.org/10.1785/0120070076` doi: 10.1785/0120070076

Rubino, V., Rosakis, A. J., & Lapusta, N. (2020). Spatiotemporal properties of sub-rayleigh and supershear ruptures inferred from full-field dynamic imaging of laboratory experiments. *Journal of Geophysical Research: Solid Earth*, *125*(2), e2019JB018922. Retrieved from `https://agupubs.onlinelibrary.wiley.com/doi/abs/10.1029/2019JB018922` (e2019JB018922 2019JB018922) doi: https://doi.org/10.1029/2019JB018922

Sato, H., Fehler, M. C., & Maeda, T. (2012). *Seismic wave propagation and scattering in the heterogeneous earth.*

Satoh, T. (2002, 04). Empirical frequency-dependent radiation pattern of the 1998 miyagiken-nanbu earthquake in japan. *Bulletin of the Seismological Society of America*, *92*(3), 1032-1039. Retrieved from `https://doi.org/10.1785/0120010153` doi: 10.1785/0120010153

Shearer, P. (2015). 1.24 - deep earth structure: Seismic scattering in the deep earth. In G. Schubert (Ed.), *Treatise on geophysics (second edition)* (Second Edition ed., p. 759-787). Oxford: Elsevier. Retrieved from `https://www.sciencedirect.com/science/article/pii/B978044453802400018X` doi: https://doi.org/10.1016/B978-0-444-53802-4.00018-X

Shi, Z., & Day, S. M. (2013). Rupture dynamics and ground motion from 3-d rough-fault simulations. *Journal of Geophysical Research: Solid Earth*, *118*(3), 1122-1141. Retrieved from `https://agupubs.onlinelibrary.wiley.com/doi/abs/10.1002/jgrb.50094` doi: https://doi.org/10.1002/jgrb.50094

Smith, E. M., & Mooney, W. D. (2021, 03). A seismic intensity survey of the 16 april 2016 mw 7.8 pedernales, ecuador, earthquake: A comparison with strong-motion data and teleseismic backprojection. *Seismological Research Letters*, *92*(4), 2156-2171. Retrieved from `https://doi.org/10.1785/0220200290` doi: 10.1785/0220200290

Somerville, P. G., Smith, N. F., Graves, R. W., & Abrahamson, N. A. (1997, 01). Modification of empirical strong ground motion attenuation relations to include the amplitude and duration effects of rupture directivity. *Seismological Research Letters*, *68*(1), 199-222. Retrieved from `https://doi.org/10.1785/gssrl.68.1.199` doi: 10.1785/gssrl.68.1.199

Spudich, P., & Frazer, L. N. (1984, 12). Use of ray theory to calculate high-frequency radiation from earthquake sources having spatially variable rupture velocity and stress drop. *Bulletin of the Seismological Society of America*, *74*(6), 2061-2082. Retrieved from `https://doi.org/10.1785/BSSA0740062061` doi: 10.1785/BSSA0740062061

Stafford, P. J. (2017, 10). Interfrequency correlations among fourier spectral ordinates and implications for stochastic ground-motion simulation. *Bulletin of the Seismological Society of America*, *107*(6), 2774-2791. Retrieved from `https://doi.org/10.1785/0120170081` doi: 10.1785/0120170081

Swanson, M. T. (2006). Pseudotachylyte-bearing strike-slip faults in mylonitic host rocks, fort foster brittle zone, kittery, maine. In *Earthquakes: Radiated energy and the physics of faulting* (p. 167-179). American Geophysical Union (AGU). Retrieved from `https://agupubs.onlinelibrary.wiley.com/doi/abs/10.1029/170GM17` doi: https://doi.org/10.1029/170GM17

Takemura, S., Furumura, T., & Maeda, T. (2015, 02). Scattering of high-frequency seismic waves caused by irregular surface topography and small-scale velocity inhomogeneity. *Geophysical Journal International*, *201*(1), 459-474. Retrieved from https://doi.org/10.1093/gji/ggv038 doi: 10.1093/gji/ggv038

Takemura, S., Furumura, T., & Saito, T. (2009, 08). Distortion of the apparent s-wave radiation pattern in the high-frequency wavefield: Tottori-ken seibu, japan, earthquake of 2000. *Geophysical Journal International*, *178*(2), 950-961. Retrieved from https://doi.org/10.1111/j.1365-246X.2009.04210.x doi: 10.1111/j.1365-246X.2009.04210.x

Takenaka, H., Mamada, Y., & Futamure, H. (2003). Near-source effect on radiation pattern of high-frequency s waves: strong sh–sv mixing observed from aftershocks of the 1997 northwestern kagoshima, japan, earthquakes. *Physics of the Earth and Planetary Interiors*, *137*(1), 31-43. Retrieved from https://www.sciencedirect.com/science/article/pii/S0031920103000062 (The quantitative prediction of strong-motion and the physics of earthquake sources) doi: https://doi.org/10.1016/S0031-9201(03)00006-2

Tan, F., Ge, Z., Kao, H., & Nissen, E. (2019, 01). Validation of the 3-d phase-weighted relative back projection technique and its application to the 2016 mw 7.8 kaikōura earthquake. *Geophysical Journal International*, *217*(1), 375-388. Retrieved from https://doi.org/10.1093/gji/ggz032 doi: 10.1093/gji/ggz032

Tan, O. (2025, Apr 01). Long-term aftershock properties of the catastrophic 6 february 2023 kahramanmaraş (türkiye) earthquake sequence. *Acta Geophysica*, *73*(2), 1023-1040. Retrieved from https://doi.org/10.1007/s11600-024-01419-y doi: 10.1007/s11600-024-01419-y

Taufiqurrahman, T., Gabriel, A.-A., Ulrich, T., Valentová, L., & Gallovič, F. (2022). Broadband dynamic rupture modeling with fractal fault roughness, frictional heterogeneity, viscoelasticity and topography: The 2016 mw 6.2 amatrice, italy earthquake. *Geophysical Research Letters*, *49*(22), e2022GL098872. Retrieved from https://agupubs.onlinelibrary.wiley.com/doi/abs/10.1029/2022GL098872 (e2022GL098872 2022GL098872) doi: https://doi.org/10.1029/2022GL098872

Tong, X., Wang, Y., & Chen, S. (2023, 11). Coseismic deformation of the 2023 türkiye earthquake doublet from sentinel-1 insar and implications for earthquake hazard. *Seismological Research Letters*, *95*(2A), 574-583. Retrieved from https://doi.org/10.1785/0220230282 doi: 10.1785/0220230282

Trugman, D. T., Chu, S. X., & Tsai, V. C. (2021). Earthquake source complexity controls the frequency dependence of near-source radiation patterns. *Geophysical Research Letters*, *48*(17), e2021GL095022. Retrieved from https://agupubs.onlinelibrary.wiley.com/doi/abs/10.1029/2021GL095022 (e2021GL095022 2021GL095022) doi: https://doi.org/10.1029/2021GL095022

Tsai, V. C., & Hirth, G. (2020). Elastic impact consequences for high-frequency earthquake ground motion. *Geophysical Research Letters*, *47*(5), e2019GL086302. Retrieved from https://agupubs.onlinelibrary.wiley.com/doi/abs/10.1029/2019GL086302 (e2019GL086302 2019GL086302) doi: https://doi.org/10.1029/2019GL086302

Tsai, V. C., Hirth, G., Trugman, D. T., & Chu, S. X. (2021). Impact versus frictional earthquake models for high-frequency radiation in complex fault zones. *Journal of Geophysical Research: Solid Earth*, *126*(8), e2021JB022313. Retrieved from https://agupubs.onlinelibrary.wiley.com/doi/abs/10.1029/2021JB022313 (e2021JB022313 2021JB022313) doi: https://doi.org/10.1029/2021JB022313

Vera, F., Tilmann, F., & Saul, J. (2024). A decade of short-period earthquake rupture histories from multi-array back-projection. *Journal of Geophysical Research: Solid Earth*, *129*(2), e2023JB027260. Retrieved from https://agupubs.onlinelibrary.wiley.com/doi/abs/10.1029/2023JB027260 (e2023JB027260 2023JB027260) doi: https://doi.org/10.1029/2023JB027260

Vidale, J. E., & Li, Y.-G. (2003, Jan 01). Damage to the shallow landers fault from the nearby hector mine earthquake. *Nature*, *421*(6922), 524-526. Retrieved from https://doi.org/10.1038/nature01354 doi: 10.1038/nature01354

Vyas, J. C., Galis, M., & Mai, P. M. (2023, 12). Ground-motion variability for ruptures on rough faults. *Bulletin of the Seismological Society of America*, *114*(2), 965-981. Retrieved from https://doi.org/10.1785/0120230117 doi: 10.1785/0120230117

Wan, Z., Dong, R., Wang, D., Xu, S., Wang, Z., & Wang, Q. (2024, 03). Along-strike variation of rupture characteristics and aftershock patterns of the 2023 mw 7.8 türkiye earthquake controlled by fault structure. *Seismological Research Letters*, *95*(4), 2071-2080. Retrieved from https://doi.org/10.1785/0220230378 doi: 10.1785/0220230378

Wang, D., Takeuchi, N., Kawakatsu, H., & Mori, J. (2016). Estimating high frequency energy radiation of large earthquakes by image deconvolution back-projection. *Earth and Planetary Science Letters*, *449*, 155-163. Retrieved from https://www.sciencedirect.com/science/article/pii/S0012821X1630276X doi: https://doi.org/10.1016/j.epsl.2016.05.051

Wang, K., Xu, X., & Hu, Y. (2024, 09). Kinematics of the 2023 kahramanmaraş earthquake doublet: Biased near-fault data and shallow slip deficit. *Seismological Research Letters*, *96*(2A), 828-837. Retrieved from https://doi.org/10.1785/0220240062 doi: 10.1785/0220240062

Wang, W., Liu, Y., Fan, X., Ma, C., & Shan, X. (2023). Coseismic deformation, fault slip distribution, and coulomb stress perturbation of the 2023 türkiye-syria earthquake doublet based on sar offset tracking. *Remote Sensing*, *15*(23). Retrieved from https://www.mdpi.com/2072-4292/15/23/5443 doi: 10.3390/rs15235443

Wang, Z., Zhang, W., Taymaz, T., He, Z., Xu, T., & Zhang, Z. (2023). Dynamic rupture process of the 2023 mw 7.8 kahramanmaraş earthquake (se türkiye): Variable rupture speed and implications for seismic hazard. *Geophysical Research Letters*, *50*(15), e2023GL104787. Retrieved from https://agupubs.onlinelibrary.wiley.com/doi/abs/10.1029/2023GL104787 (e2023GL104787 2023GL104787) doi: https://doi.org/10.1029/2023GL104787

Wei, S., Zeng, H., Shi, Q., Liu, J., Luo, H., Hu, W., ... Wang, T. (2022). Simultaneous rupture propagation through fault bifurcation of the 2021 mw7.4 maduo earthquake. *Geophysical Research Letters*, *49*(21), e2022GL100283. Retrieved from https://agupubs.onlinelibrary.wiley.com/doi/abs/10.1029/2022GL100283 (e2022GL100283 2022GL100283) doi: https://doi.org/10.1029/2022GL100283

Wells, D. L., & Coppersmith, K. J. (1994, 08). New empirical relationships among magnitude, rupture length, rupture width, rupture area, and surface displacement. *Bulletin of the Seismological Society of America*, *84*(4), 974-1002. Retrieved from https://doi.org/10.1785/BSSA0840040974 doi: 10.1785/BSSA0840040974

Withers, K. B., Olsen, K. B., Day, S. M., & Shi, Z. (2018, 11). Ground motion and intraevent variability from 3d deterministic broadband (0–7.5 hz) simulations along a nonplanar strike-slip fault. *Bulletin of the Seismological Society of America*, *109*(1), 229-250. Retrieved from https://doi.org/10.1785/0120180006 doi: 10.1785/0120180006

Withers, K. B., Olsen, K. B., Shi, Z., & Day, S. M. (2018, 11). Validation of deterministic broadband ground motion and variability from dynamic rupture simulations of buried thrust earthquakes. *Bulletin of the Seismological Society of America*, *109*(1), 212-228. Retrieved from https://doi.org/10.1785/0120180005 doi: 10.1785/0120180005

Xu, L., Mohanna, S., Meng, L., Ji, C., Ampuero, J.-P., Yunjun, Z., ... Liang, C.

(2023, Oct 17). The overall-subshear and multi-segment rupture of the 2023 mw7.8 kahramanmaraş, turkey earthquake in millennia supercycle. *Communications Earth & Environment*, *4*(1), 379. Retrieved from https://doi.org/10.1038/s43247-023-01030-x doi: 10.1038/s43247-023-01030-x

Xu, X., Sandwell, D. T., Ward, L. A., Milliner, C. W. D., Smith-Konter, B. R., Fang, P., & Bock, Y. (2020). Surface deformation associated with fractures near the 2019 ridgecrest earthquake sequence. *Science*, *370*(6516), 605-608. Retrieved from https://www.science.org/doi/abs/10.1126/science.abd1690 doi: 10.1126/science.abd1690

Xu, Y., Koper, K. D., Sufri, O., Zhu, L., & Hutko, A. R. (2009). Rupture imaging of the m 7.9 12 may 2008 wenchuan earthquake from back projection of teleseismic p waves. *Geochemistry, Geophysics, Geosystems*, *10*(4). Retrieved from https://agupubs.onlinelibrary.wiley.com/doi/abs/10.1029/2008GC002335 doi: https://doi.org/10.1029/2008GC002335

Yagi, Y., & Okuwaki, R. (2015). Integrated seismic source model of the 2015 gorkha, nepal, earthquake. *Geophysical Research Letters*, *42*(15), 6229-6235. Retrieved from https://agupubs.onlinelibrary.wiley.com/doi/abs/10.1002/2015GL064995 doi: https://doi.org/10.1002/2015GL064995

Yao, H., Gerstoft, P., Shearer, P. M., & Mecklenbräuker, C. (2011). Compressive sensing of the tohoku-oki mw 9.0 earthquake: Frequency-dependent rupture modes. *Geophysical Research Letters*, *38*(20). Retrieved from https://agupubs.onlinelibrary.wiley.com/doi/abs/10.1029/2011GL049223 doi: https://doi.org/10.1029/2011GL049223

Yao, S., & Yang, H. (2025). Rupture phases reveal geometry-related rupture propagation in a natural earthquake. *Science Advances*, *11*(4), eadq0154. Retrieved from https://www.science.org/doi/abs/10.1126/sciadv.adq0154 doi: 10.1126/sciadv.adq0154

Ye, L., Lay, T., Kanamori, H., & Rivera, L. (2016, Feb 01). Rupture characteristics of major and great (m $\geq$ 7.0) megathrust earthquakes from 1990 to 2015: 1. source parameter scaling relationships. *Journal of Geophysical Research: Solid Earth*, *121*(2), 826-844. Retrieved from https://doi.org/10.1002/2015JB012426 doi: 10.1002/2015JB012426

Yen, M.-H., Türker, E., Ulrich, T., Marchandon, M., Gabriel, A.-A., & Cotton, F. (2025, Jan 04). An analysis of directivity pulses using empirical data and dynamic rupture simulations of the 2023 kahramanmaras earthquake doublet. *Earthquake Spectra*, 87552930241305012. Retrieved from https://doi.org/10.1177/87552930241305012 doi: 10.1177/87552930241305012

Yin, J., Yang, H., Yao, H., & Weng, H. (2016). Coseismic radiation and stress drop during the 2015 m 8.3 illapel, chile megathrust earthquake. *Geophysical Research Letters*, *43*(4), 1520-1528. Retrieved from https://agupubs.onlinelibrary.wiley.com/doi/abs/10.1002/2015GL067381 doi: https://doi.org/10.1002/2015GL067381

Yue, H., & Lay, T. (2020). Resolving complicated faulting process using multi-point-source representation: Iterative inversion algorithm improvement and application to recent complex earthquakes. *Journal of Geophysical Research: Solid Earth*, *125*(2), e2019JB018601. Retrieved from https://agupubs.onlinelibrary.wiley.com/doi/abs/10.1029/2019JB018601 (e2019JB018601 2019JB018601) doi: https://doi.org/10.1029/2019JB018601

Yue, H., Shen, Z.-K., Zhao, Z., Wang, T., Cao, B., Li, Z., … Xue, L. (2022). Rupture process of the 2021 m7.4 maduo earthquake and implication for deformation mode of the songpan-ganzi terrane in tibetan plateau. *Proceedings of the National Academy of Sciences*, *119*(23), e2116445119. Retrieved from https://www.pnas.org/doi/abs/10.1073/pnas.2116445119 doi: 10.1073/pnas.2116445119

Zeng, Y., & Anderson, J. G. (1996, 02). A composite source model of the 1994 northridge earthquake using genetic algorithms. *Bulletin of the Seismological Society of America*, *86*(1B), S71-S83. Retrieved from https://doi.org/10.1785/BSSA08601B0S71 doi: 10.1785/BSSA08601B0S71

Zeng, Y., Anderson, J. G., & Su, F. (1995). Subevent rake and random scattering effects in realistic strong ground motion simulation. *Geophysical Research Letters*, *22*(1), 17-20. Retrieved from https://agupubs.onlinelibrary.wiley.com/doi/abs/10.1029/94GL02798 doi: https://doi.org/10.1029/94GL02798

Zeng, Y., Anderson, J. G., & Yu, G. (1994). A composite source model for computing realistic synthetic strong ground motions. *Geophysical Research Letters*, *21*(8), 725-728. Retrieved from https://agupubs.onlinelibrary.wiley.com/doi/abs/10.1029/94GL00367 doi: https://doi.org/10.1029/94GL00367

Zhang, H., & Ge, Z. (2010, 11). Tracking the rupture of the 2008 wenchuan earthquake by using the relative back-projection method. *Bulletin of the Seismological Society of America*, *100*(5B), 2551-2560. Retrieved from https://doi.org/10.1785/0120090243 doi: 10.1785/0120090243

Zhang, Y., Tang, X., Liu, D., Taymaz, T., Eken, T., Guo, R., … Sun, H. (2023, Nov 01). Geometric controls on cascading rupture of the 2023 kahramanmaraş earthquake doublet. *Nature Geoscience*, *16*(11), 1054-1060. Retrieved from https://doi.org/10.1038/s41561-023-01283-3 doi: 10.1038/s41561-023-01283-3